Nuclear Argonaute protein NRDE-3 switches small RNA binding partners during embryogenesis coincident with the formation of SIMR granules

Shihui Chen and Carolyn M. Phillips

Affiliations

[1] Department of Biological Sciences, University of Southern California, Los Angeles, CA 90089

Corresponding author: Carolyn M. Phillips, Department of Biological Sciences, University of Southern California, 1050 Childs Way RRI 201, Los Angeles, CA 90089-2910. Email: cphil@usc.edu

Abstract

RNA interference (RNAi) is a conserved gene regulation mechanism that utilizes the Argonaute protein and their associated small RNAs to exert regulatory function on complementary transcripts. While the majority of germline-expressed RNAi pathway components reside in perinuclear germ granules, it is unknown whether and how RNAi pathways are spatially organized in other cell types. Here we find that the small RNA biogenesis machinery is spatially and temporally organized during embryogenesis. Specifically, the RNAi factor, SIMR-1, forms visible concentrates during mid-embryogenesis that contain an RNA-dependent RNA polymerase, a poly-UG polymerase, and the unloaded nuclear Argonaute protein, NRDE-3. Further, we observe that many other RNAi factors form foci in embryonic cells distinct from SIMR granules, including the Argonaute protein CSR-1, underscoring a potential role for cytoplasmic concentrates of RNAi factors to promote gene regulation in embryos. Curiously, coincident with the appearance of the "SIMR granules", the small RNAs bound to NRDE-3 switch from predominantly CSR-class 22G-RNAs to ERGO-dependent 22G-RNAs. Thus, our study defines two separable roles for NRDE-3, targeting germline-expressed genes during early embryogenesis and switching later in embryogenesis to repress recently duplicated genes and retrotransposons in somatic cells, highlighting the plasticity of Argonaute proteins and the need for more precise temporal characterization of Argonaute-small RNA interactions.

Introduction

Precise gene expression is essential for organisms at all developmental stages. Small RNAs and their partners, the Argonaute (AGO) proteins, play an important role in regulating gene expression by targeting and silencing complementary nucleic acid sequences. This small RNA-mediated gene silencing process is known as RNA interference (RNAi) (Fire et al. 1998). The nematode *Caenorhabditis elegans*, distinguished by its expanded Argonaute family and intricate RNAi pathway, is a well-established model organism to study the RNAi pathway. *C. elegans* has 19 functional Argonaute proteins and various classes of small RNAs (Yigit et al. 2006; Seroussi et al. 2023), which is greatly expanded compared to 8 Argonaute proteins in mammals, 5 in *Drosophila melanogaster*, and 1 in *Schizosaccharomyces pombe* (Höck and Meister 2008). This expansion of the Argonaute family in nematodes may be linked to the diversity of habitats in which nematodes reside and environmental cues to which they must respond. First, RNAi has been well-studied in plants for its role as an antiviral defense mechanism (Ding et al. 2004); and like plants, worms lack an adaptive immune system, making the RNAi system a primary means to respond to viral intruders (Félix et al. 2011; Ashe et al. 2013; Sarkies and Miska 2013). Second,

nematodes have a specialized nucleic acid transporter required for the uptake of double-strand (ds)RNA from the intestinal lumen (McEwan et al. 2012; Winston et al. 2007), indicating that environmental sensing mediated by ingested dsRNA is an important aspect of nematode physiology (Sarkies and Miska 2013). Lastly, it has been proposed that Ago diversity and rapid evolution could be linked to the environmental plasticity of nematodes, including the capacity for parasitism and challenges of invading and colonizing a host (Buck and Blaxter 2013). Regardless of the evolutionary origin for the expansion of RNAi pathway proteins in nematodes, these pathways are not only important for a response to the environment, but are essential for the regulation of thousands of endogenous genes. Therefore, untangling the details of RNA silencing in *C. elegans* will shed light on the mechanisms of small RNA-mediated gene regulation in *C. elegans* and other organisms.

Argonaute proteins can be subdivided into three clades. Proteins are grouped into the AGO and PIWI clades based on their similarity to *Arabidopsis thaliana* AGO1 and *Drosophila melanogaster* PIWI, respectively. The third, WAGO, clade represents a nematode-specific expansion of the Argonaute protein family (Yigit et al. 2006). While small RNAs bound by the AGO- and PIWI-clade Argonaute proteins tend to be processed from longer, precursor transcripts, the WAGO-clade Argonaute proteins bind 22-nucleotide, 5'-triphosphorylated small RNAs (22G-RNAs) with which are each de novo synthesized by RNA-dependent RNA polymerases (RdRPs) (Gu et al. 2009; Pak and Fire 2007; Aoki et al. 2007). However, even within the WAGO clade, each of the 11 Argonaute proteins exhibits specificity for a unique group of 22G-RNAs and exhibits distinct tissue and developmental expression patterns (Seroussi et al. 2023). For example, WAGO-1 binds 22G-RNAs that target transposons, pseudogenes, and aberrant transcripts, and silences genes post-transcriptionally in the germline cytoplasm (Gu et al. 2009), while CSR-1 binds 22G-RNAs targeting germline-expressed genes, functioning to clear maternal mRNA in early embryos while licensing and tuning gene expression in the adult germline (Quarato et al. 2021; Gu et al. 2009; Claycomb et al. 2009). Other WAGO Argonautes, such as SAGO-1 and SAGO-2, function exclusively in somatic cells and play roles in regulating endogenous genes, exogenous RNAi, and immunity (Seroussi et al. 2023). Unique amongst the WAGO Argonautes for their nuclear localization are HRDE-1 and NRDE-3, which are thought to silence genes co-transcriptionally in germline and soma respectively, and are required for the inheritance of RNA silencing signals from parents to offspring (Buckley et al. 2012; Guang et al. 2008). Despite extensive characterization of the *C. elegans* Argonaute proteins, we still know little about the factors that promote the spatiotemporal expression of each Argonaute protein and the mechanisms that promote Argonaute-small RNA binding specificity. Furthermore, most

Argonaute-small RNA sequencing experiments have been performed at a single time point, usually in adult *C. elegans*, meaning that we have little understanding as to how the RNA targets of each Argonaute protein change across development.

In the *C. elegans* germline, many of the RNAi components, including Argonaute proteins, RdRPs, and other small RNA processing machinery, localize within phase-separated germ granules. Often, proteins acting in different functional branches of the RNAi pathway seem to reside in separate compartments of the germ granules, suggesting that there are specialized areas within the germ granules where distinct molecular reactions occur. Presently, four sub-compartments of the germ granule have been identified in *C. elegans*: P granules, *Mutator* foci, Z granules, and SIMR foci (Brangwynne et al. 2009; Phillips et al. 2012; Wan et al. 2018; Manage et al. 2020). These germ granule compartments are situated at the cytoplasmic side of the nucleus, proximal to nuclear pores. However, the mechanisms governing their spatial organization remain unknown. Moreover, with the majority of studies focusing on mechanisms of RNA silencing and germ granule organization in the germline, there is limited understanding of how each of these germ granule compartments assembles and functions in embryos. It has been observed that in *C. elegans* embryogenesis, the primordial germline cell P4 divides into Z2 and Z3 progenitor germ cells (PGCs) at around the 100-cell stage, coinciding with the demixing of Z granules from P granules, the appearance of *Mutator* foci and SIMR foci, and the initiation of germ cell transcription (Updike and Strome 2010; Uebel et al. 2021; Wan et al. 2018; Seydoux and Dunn 1997). Together, the assembly of this more complex germ granule organization coinciding with a burst of transcription from the germ cells, may indicate that these multi-compartment structures are necessary to monitor the newly-synthesized germline transcripts. Yet even these limited studies of RNAi pathway factors in embryos fail to address a role for ribonucleoprotein granules in RNA silencing in the soma.

Here, we discovered that SIMR-1, the founding component of the germline SIMR foci, is also found in cytoplasmic granules in the somatic cells of *C. elegans* embryos. These embryonic SIMR granules additionally contain factors involved in 22G-RNA amplification and associated with the nuclear Argonaute protein, NRDE-3. However, NRDE-3 itself only associates with the SIMR granules when not bound to small RNAs. Strikingly, the SIMR granules exhibit temporal dynamics where they first appear in early embryogenesis (around the 8-cell stage), peak around the 100-cell stage, and have mostly disappeared by the comma stage of embryogenesis. Curiously, these embryonic SIMR granules are by no means the only RNAi-related embryonic granules, as numerous other RNAi factors are found in separate granules in embryos, including components of the CSR pathway, the Argonaute CSR-1 and its RdRP EGO-1. Furthermore, by sequencing

103 the small RNAs bound by NRDE-3 in early and late embryogenesis, we found that the formation
104 of the SIMR granules coincides with a switch in NRDE-3 small RNA targets, from CSR-class 22G-
105 RNAs to ERGO-class 22G-RNAs. Together, our data demonstrates that NRDE-3 has two
106 separate functions, first acting with CSR-1 in early embryogenesis, possibly to transcriptionally
107 silence germline-expressed transcripts in somatic cells, and second acting downstream of ERGO-
108 1 to transcriptionally silence retrotransposons, pseudogenes, and aberrant transcripts. Further,
109 the SIMR granules themselves appear to be sites of NRDE-3-bound 22G-RNA biogenesis and
110 loading and may contribute to the efficiency or specificity of Argonaute-small RNA interactions
111 during embryogenesis.
112
113 **Results:**
114 **SIMR-1 and ENRI-2 localize to cytoplasmic granules during embryogenesis**
115 In previous work, we sought to identify proteins that associate with SIMR-1 and ultimately
116 found that SIMR-1 associates with HRDE-2 and the nuclear Argonaute protein, HRDE-1, to
117 promote correct HRDE-1 small RNA binding in germ cells (Chen and Phillips 2024). In that work,
118 we also identified another nuclear Argonaute protein, NRDE-3, as an interactor of SIMR-1. To
119 delve further into this potential interaction between SIMR-1 and NRDE-3, we first systematically
120 compiled a list of the protein interactions identified from previous studies for both SIMR-1 and
121 NRDE-3 (Fig. 1A). Interestingly, the HRDE-2 paralog, ENRI-2, had been shown to interact with
122 both SIMR-1 and NRDE-3 in embryos by immunoprecipitation followed by mass spectrometry (IP
123 mass-spec), and another HRDE-2 paralog, ENRI-1, was similarly shown to interact with only
124 NRDE-3 (Lewis et al. 2020). These findings suggest that SIMR-1, NRDE-3, ENRI-2, and possibly
125 ENRI-1 proteins may function together in the somatic nuclear RNAi pathway, analogous to the
126 roles of SIMR-1, HRDE-1, and HRDE-2 in the germline nuclear RNAi pathway.
127 Here, we first aimed to address whether and where NRDE-3, SIMR-1, ENRI-1, and ENRI-
128 2 colocalize. NRDE-3 has previously been shown to be expressed in the nucleus of most somatic
129 cells (Guang et al. 2008). Until recently, all characterization of NRDE-3 was done using a low-
130 copy, integrated transgenic strain in which the nuclear localization was not visible until the ~30-
131 80-cell stage of development, and it was presumed that this localization reflected the endogenous
132 NRDE-3 localization (Guang et al. 2008; Lewis et al. 2020). However, a more recent study
133 constructed an endogenously-tagged NRDE-3 strain using CRISPR and found that NRDE-3
134 additionally localizes to the nucleus of oocytes and early embryos (Seroussi et al. 2023, 2022),
135 suggesting that the older, transgenic NRDE-3 construct may be targeted for silencing in germ
136 cells. SIMR-1 is a component of the SIMR foci, a sub-compartment of germ granules, that appears

as punctate foci at the periphery of *C. elegans* germ cells starting in embryos through the adult stage (Manage et al. 2020; Uebel et al. 2021). ENRI-1 has been reported to localize to the cytoplasm of oocytes and embryos while ENRI-2 localized to both the nucleus and cytoplasm, varying depending on developmental stage (Lewis et al. 2020). With these four proteins showing distinct localization patterns from one another, it was unclear how these proteins could physically interact.

To investigate where and how these interactions might potentially occur, we chose to initially examine localization of these proteins in the germline of adult *C. elegans* using the endogenously-tagged NRDE-3 strain which is visible starting in late pachytene. As expected based on previous work, NRDE-3 localizes to the nucleus of germ cells, while SIMR-1 is found in the cytoplasm in SIMR foci, a compartment of the germ granule (Supplementary Fig. 1A) (Seroussi et al. 2022, 2023; Manage et al. 2020). Next, we decided to examine NRDE-3 and SIMR-1 localization in embryos, carefully dividing the embryos into distinct developmental stages, from 4-cell to comma stage. As expected, we found that NRDE-3 is consistently localized to the nucleus in all embryonic stages (Fig. 1B). Interestingly, we observed that SIMR-1 forms granules in the cytoplasm of somatic cells during some embryonic stages (Fig. 1B). By quantifying the total number of granules per embryo across embryonic development, we found that the SIMR-1 granules first appear around the 8-cell stage and reach a peak at approximately the 100-cell stage, coinciding with the division of the germline precursor cell P_4 into the primordial germ cells Z_2 and Z_3 (Wang and Seydoux 2013). Subsequently, the number of SIMR-1 granules decreases, and in late embryos, SIMR-1 localizes primarily to the germ granules surrounding the two germ cells, as previously observed (Uebel et al. 2021) (Fig. 1B,C). We had previously shown that the Tudor domain of SIMR-1 was important for its assembly into germline SIMR foci. Therefore, we next explored the requirement for the Tudor domain in assembling SIMR-1 cytoplasmic granules in embryos (Manage et al. 2020). We found that the Tudor domain mutant, SIMR-1(R159C), fails to assemble in cytoplasmic granules in the embryos (Supplementary Fig. 1B), indicating that, similar to germline SIMR foci, the Tudor domain is also required for assembly of the cytoplasmic SIMR granules in embryos.

We next focused on ENRI-1 and ENRI-2 and observed that ENRI-2 shows similar cytoplasmic granule localization and colocalizes with SIMR-1 in embryos, but it does not localize to the germ granules in Z_2 and Z_3, suggesting that the activity of ENRI-2 is restricted to somatic cells (Fig. 1B). Finally, we examined the localization N-terminal tagged 2xTy1::GFP::ENRI-1, and found that we could not detect any specific localization in either nuclei or cytoplasmic granules (Supplementary Fig. 1C) (Lewis et al. 2020). Consequently, we constructed a new strain with C

terminal tagged ENRI-1::mCherry::2xHA and confirmed the presence of full-length ENRI-1 protein with Western Blot (Supplementary Fig. 1D). Nonetheless, we could not detect any ENRI-1 localization in embryos with our newly generated strain (Supplementary Fig. 1C). These results are consistent with the fact that ENRI-1 does not interact directly with either SIMR-1 or ENRI-2 by immunoprecipitation (Fig. 1A) (Lewis et al. 2020). Altogether, these data indicate that SIMR-1 and ENRI-2 colocalize at cytoplasmic granules in the somatic cells of embryos and suggest that ENRI-2 and SIMR-1 may function together at these sites. In contrast, NRDE-3 is spatially separated in the nucleus and no clear expression pattern was observed for ENRI-1.

Unloaded NRDE-3 associates with SIMR-1 in cytoplasmic granules

Next, to determine whether SIMR-1 and ENRI-2 are required for NRDE-3 localization, we introduced the *simr-1* mutant, *enri-2* mutant, *enri-1* mutant, and *enri-1; enri-2* double mutant in the endogenously tagged GFP::3xFLAG::NRDE-3 strain, and examined NRDE-3 localization across embryonic developmental stages. We observed no changes in NRDE-3 expression or nuclear localization in any of the mutants examined at any developmental stage (Supplementary Fig. 2A).

In previous work, we demonstrated that the germline nuclear Argonaute protein HRDE-1 loses nuclear localization and associates in the cytoplasm with the SIMR compartment of germ granules when it is unable to bind small RNAs (Chen and Phillips 2024). Additionally, ENRI-2 interacts more strongly with NRDE-3 in an *eri-1* mutant background compared to wild-type (Lewis et al. 2020), suggesting that the interaction occurs when NRDE-3 does not bind small RNAs. Localization of unloaded NRDE-3 has been examined in the seam cells of L3 stage animals, where, like HRDE-1, it loses nuclear localization and becomes restricted to the cytoplasm (Guang et al. 2008). Therefore, we next sought to examine the localization of NRDE-3 when it is unbound to small RNA in embryos and germline. First, we aimed to deplete the preferred small RNA binding partners of NRDE-3. NRDE-3 has previously been shown to bind secondary 22G-RNAs downstream of ERGO-class 26G-RNAs, dependent on ERI-1, which is required for 26G-RNA biogenesis (Guang et al. 2008; Han et al. 2009; Seroussi et al. 2023), and RDE-3/MUT-2, which is a component of the *Mutator* complex and necessary for 22G-RNA production (Chen et al. 2005; Phillips et al. 2012, 2014). Therefore, we introduced an *eri-1* mutant and a *rde-3/mut-2* mutant into the endogenously GFP-tagged NRDE-3 background. We observed that NRDE-3 associates with somatic granules with a similar spatiotemporal pattern to SIMR-1 and ENRI-2, peaking around the 100-cell stage, although the total number of granules per embryo is lower for NRDE-3 granules in the *eri-1* and *rde-3/mut-2* mutant backgrounds compared to SIMR granules (Fig.

2A,B). Next, to fully abolish the small RNA binding capacity of NRDE-3 and to confirm that the observed granule localization was due to the loss of small RNA loading, we introduced mutations to abolish small RNA binding into the GFP-tagged NRDE-3; specifically, residues 687H and 691K in the Mid domain were mutated to alanine, hereafter referred to as NRDE-3(HK-AA) (Ma et al. 2005; Guang et al. 2008; Chen and Phillips 2024). NRDE-3(HK-AA) localizes exclusively to the cytoplasm across embryonic development and in the adult germline, accumulating in somatic granules at 100-cell stage similar to SIMR-1 and ENRI-2 (Fig. 2A). Quantification of the number of NRDE-3 granules per embryo in the NRDE-3(HK-AA) strain shows that the dynamics of NRDE-3 granule appearance and disappearance are similar to that of SIMR-1, where the number of granules increases from early embryos up until about 100-cell stage and then decreases as the embryos progress to later stages of development (Fig. 2C). Overall the total number of NRDE-3(HK-AA) granules quantified per embryo are similar to or modestly higher than SIMR-1 granules (Fig. 1C, Fig. 2B,C). It is also worth noting that despite the similarity in timing of NRDE-3 granule appearance and disappearance in the *eri-1* and *rde-3* mutants compared to the *nrde-3(HK-AA)* mutant, we observed a striking difference in the NRDE-3 localization in early embryos. Specifically, in *eri-1* and *rde-3* mutants, NRDE-3 localizes to the nucleus in early embryos while NRDE-3(HK-AA) localizes exclusively to the cytoplasm (Fig. 2A). Similarly, in the Z2 and Z3 primordial germ cells of late embryos, NRDE-3 is still found in the nucleus in *eri-1* and *rde-3* mutants. In contrast, NRDE-3 localizes exclusively to the cytoplasm in the somatic cells of late embryos of all three mutants. Regardless, these data indicate that NRDE-3 forms granules in the cytoplasm of somatic cells when not associated with a small RNA binding partner.

To determine whether unloaded NRDE-3 localizes to SIMR-1 granules, we examined the localization of SIMR-1 and NRDE-3 together in the *nrde-3(HK-AA)* mutant and *eri-1* mutant backgrounds. We found that SIMR-1 colocalizes perfectly with unloaded NRDE-3 in embryonic granules (Fig. 2D, Supplementary Fig. 2B). Further, the SIMR-1 granules in the *nrde-3(HK-AA)* mutant background exhibit dynamics similar to the wild-type background (Supplementary Fig. 2C), indicating that *nrde-3(HK-AA)* does not affect the localization of SIMR-1. Interestingly, NRDE-3(HK-AA) does not form granules in germ cells and is instead present exclusively in the cytoplasm, thus it does not colocalize with the SIMR compartment of germ granules (Supplementary Fig. 2D). These results demonstrate that unloaded NRDE-3 associates with SIMR-1 and ENRI-2 in cytoplasmic granules in the somatic cells of *C. elegans* embryos, indicating a potential role for SIMR-1 in the NRDE-3 nuclear RNAi pathway.

SIMR-1 and ENRI-2 recruits unloaded NRDE-3 to cytoplasmic granules

239 As previously described, unloaded NRDE-3 localizes to cytoplasmic granules in embryos
240 and colocalizes with SIMR-1. Next, we aimed to determine whether SIMR-1 and ENRI-2 are
241 required for the NRDE-3 granule localization. To this end, we introduced a *simr-1* mutant and an
242 *enri-2* mutant into the GFP-tagged NRDE-3(HK-AA) strain and assessed NRDE-3(HK-AA)
243 localization. Strikingly, we found that NRDE-3(HK-AA) granules disappear completely and NRDE-
244 3(HK-AA) is instead found exclusively in the cytoplasm in all cells across all embryonic stages
245 (Fig. 3A). Similarly, in a *simr-1; eri-1* double mutant, NRDE-3 granules are absent though NRDE-
246 3 remains in the nucleus in early embryos (Fig. 3A), similar to NRDE-3 expression in the *eri-1*
247 single mutant (Fig. 2A). These results demonstrate that both SIMR-1 and ENRI-2 are required for
248 the recruitment of NRDE-3 to cytoplasmic granules.
249 In addition, to assess whether ENRI-1 plays a role in the accumulation of unloaded NRDE-
250 3 in cytoplasmic granules, we introduced an *enri-1* mutant into the GFP-tagged NRDE-3(HK-AA)
251 strain and found that NRDE-3 association with cytoplasmic granules was not disrupted
252 (Supplementary Fig. 3A). We further examined NRDE-3(HK-AA) granule association in the *enri-*
253 *1; enri-2* double mutant and found it to be fully cytoplasmic, indistinguishable from the *enri-2* single
254 mutant (Supplementary Fig. 3A). While we had already determined that ENRI-1::mCherry did not
255 form visible foci in embryos; to rule out the possibility of partial redundancy between ENRI-1 and
256 ENRI-2, we introduced an *enri-2* mutant into the mCherry-tagged ENRI-1 strain but still unable to
257 detect any distinct ENRI-1 expression (Supplementary Fig. 3B). Lastly, to determine if NRDE-3
258 recruitment to granules could alter ENRI-1 localization, we introduced the mCherry-tagged ENRI-
259 1 into the GFP-tagged NRDE-3(HK-AA) strain, and still we could not see any granule localization
260 for ENRI-1 (Supplementary Fig. 3C). Therefore, we conclude that ENRI-1 does not function with
261 SIMR-1, ENRI-2, and NRDE-3 at cytoplasmic granules in embryos and we excluded ENRI-1 from
262 further investigation.
263 To investigate the dependence of SIMR-1 and ENRI-2 on one another, we examined
264 ENRI-2 localization in a *simr-1* mutant and SIMR-1 localization in an *enri-2* mutant. We found that
265 ENRI-2 granules are lost in the *simr-1* mutant, while SIMR-1 granules are still present in the *enri-*
266 *2* mutant, indicating that SIMR-1 functions upstream of ENRI-2 for granule assembly (Fig. 3B).
267 Therefore, we conclude that SIMR-1 and ENRI-2, but not ENRI-1, recruit unloaded NRDE-3 to
268 cytoplasmic granules, with SIMR-1 also acting to recruit ENRI-2.
269
270 **SIMR-1 does not localize to P bodies or other previously identified embryonic granules**
271 A variety of RNA-associated proteins have previously been shown to form granules in *C.*
272 *elegans* embryos. To determine whether the SIMR-1, ENRI-2, and unloaded NRDE-3 granules

273 that we have observed coincide with a previously identified granule, we examined the
274 colocalization between SIMR-1 and all other embryonic granule-associated proteins that we could
275 identify. It is well known that Processing (P) bodies, the condensates of translationally inactive
276 mRNAs and proteins, localize to cytoplasmic foci of soma in *C. elegans* embryos (Parker and
277 Sheth 2007; Gallo et al. 2008). To examine if the SIMR-1 cytoplasmic granules are P bodies, we
278 examined the localization of SIMR-1 and CGH-1, a core P body component, using a strain
279 expressing GFP-tagged SIMR-1 and mCherry-tagged CGH-1 (Du et al. 2023). We found that
280 CGH-1 does not colocalize with SIMR-1 (Supplementary Fig. 4A). CGH-1 also does not colocalize
281 with NRDE-3 cytoplasmic granules in the *eri-1* mutant (Supplementary Fig. 4B). Together, these
282 data indicate that the cytoplasmic SIMR-1 granules found in embryos are not P bodies.

283 Next, we examined two proteins previously shown to colocalize with SIMR foci in the germ
284 cells of adult animals, RSD-2 and HRDE-2 (Manage et al. 2020; Chen and Phillips 2024). RSD-2
285 is a small RNA factor required for the response to low doses of exogenously-introduced double-
286 stranded RNA (Sakaguchi et al. 2014; Han et al. 2008; Tijsterman et al. 2004; Zhang et al. 2012)
287 and HRDE-2 is a factor critical for RNAi inheritance that promotes correct small RNA loading into
288 the nuclear Argonaute HRDE-1 (Chen and Phillips 2024; Spracklin et al. 2017). However, we did
289 not observe any granule localization for RSD-2 and HRDE-2 in embryos (Supplementary Fig.
290 4C,D). In addition, SIMR-1 cytoplasmic granules were not affected by the loss of *hrde-2*
291 (Supplementary Fig. 4E). These results suggest that HRDE-2 and RSD-2 do not function together
292 with SIMR-1, ENRI-2, and NRDE-3 in embryonic granules.

293 RDE-12 interacts with Argonaute proteins and RNAi-targeted mRNAs, and has also been
294 shown to localize to cytoplasmic granules in the somatic cells of *C. elegans* embryos (Shirayama
295 et al. 2014; Yang et al. 2014). We next assessed the localization of mCherry-tagged SIMR-1
296 relative to GFP-tagged RDE-12 and found that they do not colocalize (Supplementary Fig. 4F).
297 RSD-6 is a Tudor domain-containing RNAi factor that partially colocalizes with RDE-12 in the R2
298 bodies in adult germ cells (Yang et al. 2014; Sakaguchi et al. 2014; Zhang et al. 2012). We
299 examined the expression of GFP-tagged RSD-6 in embryos and, while we did observe RSD-6 at
300 granules in somatic cells, no colocalization with mCherry-tagged SIMR-1 could be detected
301 (Supplementary Fig. 4G). The RNAi-inheritance factor and defining member of the Z compartment
302 of the germ granule, ZNFX-1, has also been observed in cytoplasmic granules in the somatic cells
303 of embryos (Wan et al. 2018; Ouyang et al. 2019), however these somatic ZNFX-1 granules also
304 fail to colocalize with SIMR-1 (Supplementary Fig. 4H). Altogether, we found that SIMR-1 fails to
305 localize to any previously characterized embryonic granules. These results further indicate that

306 there are numerous granule-localized proteins in the somatic cells of embryos, such as RDE-12,
307 RSD-6, and ZNFX-1, which may play important roles in the RNA biology of early embryos.
308
309 **Multiple *Mutator* complex proteins localize to SIMR-1 granules in embryos**
310 *Mutator* foci localize adjacent to SIMR foci in the adult germline (Manage et al. 2020; Chen
311 and Phillips 2024), so we next investigated the localization of *Mutator* components in embryos.
312 We first examined *Mutator* foci component RDE-3/MUT-2, a poly(UG) polymerase required for
313 WAGO-class 22G-RNA production (Phillips et al. 2012; Shukla et al. 2020) and found that GFP-
314 tagged RDE-3 is prominently localized to cytoplasmic granules in embryos that colocalize with
315 SIMR-1 (Fig. 4A). This colocalization led us to the hypothesis that SIMR-1 cytoplasmic granules
316 are sites of WAGO-class 22G-RNA biogenesis. Therefore, we speculated that more small RNA
317 production machinery might be localized with SIMR-1 at these cytoplasmic granules. We next
318 examined the RNA-dependent-RNA-polymerase (RdRP) RRF-1, which synthesizes WAGO-class
319 22G-RNAs and localizes to *Mutator* foci in the adult germline (Sijen et al. 2001; Gent et al. 2010;
320 Vasale et al. 2010; Phillips et al. 2012). As we predicted, RRF-1 also colocalizes with SIMR-1 in
321 somatic granules (Fig. 4B), and it fails to localize to somatic granules in the *simr-1* mutant (Fig.
322 4C).
323 MUT-16 is the scaffolding protein for germline *Mutator* foci, thus we next investigated
324 whether MUT-16 similarly scaffolds the cytoplasmic SIMR-1 granules in early embryos (Phillips
325 et al. 2012). We found that MUT-16 can be observed in cytoplasmic granules in the embryonic
326 somatic cells (Supplementary Fig. 4I), similar to what has been observed in a previous study
327 (Ouyang et al. 2019), and both SIMR-1 and RDE-3 fail to assemble into cytoplasmic granules in
328 the *mut-16* mutant (Fig. 4D, Supplementary Fig. 4J). Notably, the germ granule association of
329 SIMR-1 is unaffected, as SIMR-1 still localizes to germ granules at comma stage embryos and in
330 the adult germline (Fig. 4D) (Manage et al. 2020). Together, these data indicate that MUT-16
331 functions upstream of SIMR-1 and mediates the assembly of cytoplasmic granules in embryos. It
332 is curious to note that, in a *mut-16* mutant where SIMR-1 association with cytoplasmic granules
333 is lost in the somatic cells, SIMR-1 instead associates with mitotic spindles (Fig. 4D). To conclude,
334 we have shown that the SIMR granules found in the somatic cells of early embryos contain the
335 biogenesis machinery for WAGO-class 22G-RNAs, including RDE-3 and RRF-1, and depend on
336 the scaffolding protein MUT-16 for assembly (Fig. 4I). The differential requirement for MUT-16 on
337 the assembly of somatic SIMR-1 granules and the SIMR compartment of germ granules highlights
338 a key difference between these two compartments, which have some parallel functions but distinct
339 composition.

340

341 **CSR-1 and EGO-1 associate with a distinct type of granule in early embryos**

342 The Argonaute protein CSR-1 has also been previously seen at cytoplasmic granules in
343 the soma of early embryos, a time at which CSR-1 is functioning to clear maternal-inherited
344 mRNAs (Quarato et al. 2021; Seroussi et al. 2023; Ouyang et al. 2019). Using a GFP-tagged
345 CSR-1 strain we constructed previously (Nguyen and Phillips 2021), we confirmed that CSR-1
346 forms prominent cytoplasmic granules in embryos visible prior to the 4-cell stage and present
347 through 100-cell stage embryos, but disappear by the 200-cell stage, at which point only germ
348 granule localization is visible (Fig. 4E). Quantification of the total number of CSR-1 granules per
349 embryo across development shows that the CSR-1 granules are more abundant than the SIMR-
350 1 and NRDE-3(HK-AA) granules and differ in the timing of their appearance and disappearance
351 relative to SIMR-1 and NRDE-3(HK-AA) granules (Fig. 1C, 2C, 4F). Specifically, CSR-1 granules
352 appear earlier and peak at the 28-cell stage, while SIMR-1 and NRDE-3(HK-AA) granules appear
353 between 8- and 28-cell stages and peak at the 100-cell stage (Fig. 1C, 2C, 4F). The small RNAs
354 bound by CSR-1 are synthesized by the RdRP, EGO-1, so we next assessed the localization of
355 EGO-1 in early embryos. We found that EGO-1 colocalizes with CSR-1 in the somatic CSR-1
356 granules (Fig. 4G) and neither CSR-1 nor EGO-1 fully colocalizes with SIMR-1, although we
357 occasionally observed adjacent localization between SIMR-1 and CSR-1 (Fig. 4H, supplementary
358 Fig. 4K). Lastly, unlike RRF-1 which requires SIMR-1 to localize to embryonic foci, EGO-1
359 localizes to cytoplasmic granules in the absence of *simr-1* (Fig. 4C). Together, our results show
360 that the RdRPs, RRF-1 and EGO-1, localize to different cytoplasmic granules in the somatic cells
361 of *C. elegans* embryos, where they colocalize with Argonaute proteins, NRDE-3 and CSR-1,
362 respectively. Thus, we postulate that WAGO-class and CSR-class 22G-RNA biogenesis and
363 loading are compartmentalized into cytoplasmic granules, differing from one another both spatially
364 and temporally, in the somatic cells of early embryos (Fig. 4I).

365

366 **NRDE-3 switches small RNA partners during embryonic development**

367 The nuclear localization of NRDE-3 in the somatic cells of larvae depends on ERGO-1
368 and other proteins required for the biogenesis of ERGO-class 26G-RNAs (Guang et al. 2008).
369 Sequencing of NRDE-3-bound 22G-RNAs at the L4 to young adult transition identifies a set of
370 endogenous targets that overlaps substantially with those of ERGO-1 (Seroussi et al. 2023).
371 Together, these data have led to the conclusion that NRDE-3 acts downstream of ERGO-1 to
372 transcriptionally silence ERGO-target genes. Yet our data looking at the nuclear localization of
373 NRDE-3 in embryos, demonstrate that this model may be an incomplete picture. Specifically, in

374 *eri-1* and *rde-3* mutants where 26G-RNA or WAGO-class 22G-RNA biogenesis are abolished,
375 respectively, NRDE-3 remains localized to the nucleus in early embryos (Fig. 2A). The small RNA
376 binding-defective NRDE-3(HK-AA) is localized exclusively to the cytoplasm at the same time
377 point, indicating that small RNA binding is critical for nuclear import at this stage (Fig. 2A).
378 Accordingly, we must postulate that NRDE-3 binds another class of small RNA to promote nuclear
379 entry in very early embryos. To investigate the identity of NRDE-3-bound small RNAs across
380 embryonic development and to explore the role of the SIMR-1 granules in promoting NRDE-3
381 small RNA binding, we immunoprecipitated NRDE-3 and sequenced associated small RNAs (IP-
382 sRNA seq) in early embryos (<=100-cell) and late embryos (>=300-cell) in wild-type, *eri-1* mutant,
383 *simr-1* mutant, and *enri-2* mutant animals (Fig. 5A).

384 Prior to analyzing our data, we sought to better define the expected NRDE-3-bound small
385 RNAs. We initially planned to use two previously defined ERGO-target gene lists: the first list
386 (ERGO - Manage) is defined by small RNAs significantly depleted at least two-fold in *ergo-1*
387 mutant compared to wild-type at the gravid adult stage, with at least 10 reads per million (RPM)
388 in wild-type samples and a DESeq2 adjusted p-value of <0.05 (Manage et al. 2020); the second
389 list (ERGO - Fischer) is defined by genes reduced by 67% in *eri-7* adults or an average of 67% in
390 *ergo-1, eri-1, eri-6,* and *eri-7* embryos, with at least 10 RPM in wild-type (Fischer et al. 2011).
391 However, small RNAs targeting many of these previously defined ERGO targets were not
392 enriched by NRDE-3 in a published NRDE-3 IP-sRNA seq data on young adult animals that have
393 begun oogenesis but do not yet have embryos (Seroussi et al. 2023) (Supplementary Fig. 5A,B).
394 To define a more stringent NRDE-3-target gene list at the young adult stage, we chose genes
395 with at least four-fold enrichment ($\log_2$FC ≥2) and 100 RPM (RPM ≥100) from the NRDE-3 IP-
396 sRNA seq in young adults (Seroussi et al. 2023). This new list contains 119 genes and largely
397 overlaps with the two previously defined ERGO-target gene lists (Supplementary Fig. 5C,D). To
398 further confirm that this newly defined gene list represents NRDE-3 targets, we analyzed
399 published small RNA and mRNA sequencing data from wild-type and *nrde-3* mutant mixed-stage
400 embryos (before the bean stage) (Padeken et al. 2021). Compared to the Manage and Fischer
401 ERGO-target gene lists, the NRDE-3-target gene list shows more significant small RNA depletion
402 and a greater increase in mRNA expression in the *nrde-3* mutant compared to wild-type
403 (Supplementary Fig. 5A-C,E,F). Therefore, we use the new NRDE-3-target gene list to represent
404 the ERGO-1 pathway-dependent, NRDE-3-target genes (referred to here as ERGO targets) in
405 the rest of this study (Supplementary Table 4).

406 We next examined the small RNAs bound to NRDE-3 in wild-type early embryos and late
407 embryos, comparing our data to the published NRDE-3 IP-sRNA seq data on young adult animals

408 (Seroussi et al. 2023). Strikingly, we found that in early embryos, the majority of small RNAs
409 bound by NRDE-3 are CSR-class 22G-RNAs, which become progressively less enriched as the
410 animals develop into late embryos and then young adults (Fig. 5B-D). In contrast, enrichment for
411 small RNAs targeting ERGO-target genes increases as *C. elegans* develops, and they become
412 the majority of NRDE-3-bound small RNAs by young adulthood (Fig. 5B-D). NRDE-3 also binds
413 to CSR-target genes in the early embryos of the *eri-1* mutant, when it is observed to localize to
414 the nucleus, indicating that the production of these NRDE-3-bound CSR-class 22G-RNAs is
415 independent of *eri-1* and that CSR-class 22G-RNAs are likely sufficient to promote nuclear entry
416 of NRDE-3 in the early embryo (Fig. 2A, 5E). To conclude, NRDE-3 binds to CSR-class 22G-RNA
417 in early embryos but switches to bind preferentially to ERGO-dependent 22G-RNA in late
418 embryos and young adults, suggesting that NRDE-3 may have two separable functions at distinct
419 developmental time points. It is also curious to note that the change in small RNA preference of
420 NRDE-3 coincides with the appearance and disappearance of the cytoplasmic SIMR granules,
421 suggesting a role for SIMR-1 and ENRI-2 in promoting the loading of NRDE-3 with ERGO-
422 dependent 22G-RNAs.
423

424 **SIMR-1 and ENRI-2 are not absolutely required to promote NRDE-3 small RNA specificity**

425 Since ERGO-dependent 22G-RNA loading was mainly observed in late embryos, we
426 focused on NRDE-3-bound small RNAs in the *eri-1* mutant, *simr-1* mutant, and *enri-2* mutant late
427 embryos to determine the role of SIMR-1 granules in promoting NRDE-3 small RNA binding
428 specificity. We first examined the levels of ERGO-dependent small RNAs in the total small RNA
429 samples and observed depletion of small RNAs mapping to ERGO-target genes in the *eri-1*
430 mutant (Fig. 5E,F). This result is consistent with previous research indicating that ERI-1 is required
431 for ERGO-class 26G RNA production and downstream ERGO-dependent 22G-RNA production
432 (Vasale et al. 2010; Han et al. 2009; Guang et al. 2008). ERGO-dependent small RNAs are not
433 substantially depleted in *simr-1* or *enri-2* mutants, indicating that RRF-1 can still synthesize a
434 similar amount of ERGO-dependent 22G-RNAs when the cytoplasmic SIMR granules are absent
435 (Fig. 5F,G). Following NRDE-3 immunoprecipitation, we similarly observed a reduction in NRDE-
436 3 binding to ERGO-dependent small RNAs in the *eri-1* mutant while no significant reduction in
437 NRDE-3 binding to ERGO-dependent small RNAs was observed in either *simr-1* or *enri-2* mutants
438 (Fig. 5G,H). These results indicate that SIMR-1 and ENRI-2 are not absolutely required for the
439 production of the ERGO-dependent small RNAs during embryogenesis and the loading of these
440 small RNAs into NRDE-3. Nonetheless, since unloaded NRDE-3 and the small RNA biogenesis
441 machinery RRF-1 are dispersed to the cytoplasm in the *simr-1* mutant (Fig. 3A, 4C), NRDE-3 may

still be able to load the ERGO-dependent 22G-RNAs synthesized by RRF-1 but perhaps with lower efficiency.

NRDE-3 binds to CSR-class 22G-RNAs in germ cells and early embryos

Our foregoing results show that NRDE-3 localizes to the nucleus in early embryos independent of ERGO-dependent 22G-RNAs and binds to CSR-class 22G-RNA at this developmental stage (Fig. 2A, Fig. 5B-E). Interestingly, in late embryos from *eri-1* mutant and *rde-3* mutant, we have observed nuclear localization of NRDE-3 only in the primordial germ cells (Fig. 2A), raising an intriguing hypothesis that NRDE-3 might bind to CSR-class 22G-RNAs in germ cells throughout development and inherit NRDE-3-bound CSR-class 22G-RNAs to early embryos.

To test this hypothesis, we first asked whether the nuclear localization of NRDE-3 in the adult germline depends on ERI-1 and RDE-3. We found that NRDE-3 localizes to the nuclei of pachytene germ cells and oocytes in wild-type, *eri-1* mutants, and *rde-3* mutants, but is restricted to the cytoplasm in *nrde-3(HK-AA)* small RNA binding mutants, consistent with our observations of NRDE-3 localization in early embryos (Fig. 6A). Next, to confirm that NRDE-3 binds to CSR-class 22G-RNAs in germ cells and early embryos, we utilized auxin-inducible degron (AID) system to deplete the RdRP EGO-1 by growing the worms on 4mM auxin plates starting at the L1 stage (Zhang et al. 2015) (supplementary Fig. 6A). Surprisingly, NRDE-3 still localizes to nuclei in both germ cells and early embryos upon EGO-1 depletion (supplementary Fig. 6B), indicating that NRDE-3 either does not exclusively bind CSR-class 22G-RNAs in the germline, or NRDE-3 has the capacity to bind other small RNAs when the CSR-class 22G-RNAs are absent. We did observe some NRDE-3 localization to cytoplasmic granules in a subset of 8-cell stage embryos following EGO-1 depletion (supplementary Fig. 6B), suggesting that a proportion of NRDE-3 might be unloaded. To further probe which small RNAs NRDE-3 binds to in the germline, we introduced a *rde-3* mutation into the GFP::NRDE-3; degron::EGO-1 strain to deplete WAGO-class 22G-RNAs. We observed that NRDE-3 no longer localizes to the nucleus in both germline and early embryos in the absence of both WAGO-class 22G-RNAs and CSR-class 22G-RNAs (Fig. 6B). These results, in combination with our sequencing data, indicate that NRDE-3 likely binds CSR-class 22G-RNAs in the germline and early embryos but has the capacity to additionally bind WAGO-class 22G-RNAs when CSR-class 22G-RNAs are depleted. Furthermore, because somatic transcription is thought to initiate around the 4-cell stage (Seydoux and Fire 1994), the correlation of NRDE-3 localization between oocytes and early embryos suggests that NRDE-3, loaded with CSR-class 22G-RNAs, is likely inherited by the early embryo from the parental germline.

476 We next sought to assess the degree to which NRDE-3-bound 22G-RNAs are similar to
477 CSR-1-bound 22G-RNAs in early embryos. First, we examined the overlap of NRDE-3-targeted
478 genes in early embryos with CSR-1-targeted genes in embryos or young adult animals. We found
479 that the genes targeted by NRDE-3 substantially overlap with CSR-target genes at both stages
480 (Fig. 6C) (Quarato et al. 2021; Nguyen and Phillips 2021). Furthermore, the CSR-target genes
481 yielding the highest abundance of CSR-1-bound small RNAs in embryos also have the highest
482 abundance of NRDE-3-bound small RNAs (Supplementary Fig. 6C). These CSR-target genes
483 with highly abundant CSR-bound small RNAs are highly enriched by NRDE-3 only in embryos
484 and not in young adults (Supplementary Fig. 6C). Next, CSR-class 22G-RNAs tend to be enriched
485 at the 3' ends of mRNAs while WAGO-class 22G-RNAs are more evenly distributed across the
486 gene bodies in adult animals (Ishidate et al. 2018; Singh et al. 2021). Comparing NRDE-3-bound
487 small RNAs from early embryos to a published dataset of CSR-1-bound small RNA from mixed-
488 stage embryos, we found that both NRDE-3 and CSR-1 are heavily enriched for small RNAs
489 derived from the 3' ends of CSR-target genes in embryos (Fig. 6D). Interestingly, in adult animals,
490 CSR-1-bound 22G-RNAs are still enriched for small RNA derived from the 3' end of CSR-target
491 genes, however there is additionally a much higher enrichment of small RNAs derived from the
492 gene bodies compared to in embryos (Fig. 6D). It has previously been proposed that two types of
493 CSR-class 22G-RNAs exist, those that depend on CSR-1 catalytic activity for their production and
494 are derived primarily from target gene bodies, and those that are produced independently of CSR-
495 1 catalytic activity and are derived primarily from target 3'UTRs (Singh et al. 2021). Our data
496 points to both NRDE-3 and CSR-1 binding only the latter, CSR-1 catalytic activity-independent,
497 type of CSR-class 22G-RNA in early embryos. In contrast, NRDE-3 does not show enrichment
498 for small RNAs derived from the 3' ends of ERGO target genes in embryos, and rather the small
499 RNAs are distributed more evenly across the gene bodies (Supplementary Fig. 6D). CSR-1
500 utilizes its catalytic activity to slice and clear maternally-inherited mRNAs from early embryos,
501 preferentially binding to transcripts degraded early in embryogenesis (Quarato et al. 2021). We
502 further demonstrate that NRDE-3 similarly binds preferentially to early-degraded transcripts,
503 suggesting it may be functioning in parallel to CSR-1 (Fig. 6E). Lastly, the expression of mRNAs
504 targeted by CSR-1 decreases across embryonic development as CSR-1 actively slices and clears
505 these maternal transcripts (Quarato et al. 2021). We similarly find that the mRNAs targeted by
506 NRDE-3 in young embryos, which correspond primarily to CSR-target mRNAs, decrease in
507 expression across development, while its targets in young adults, corresponding primarily to
508 ERGO-target mRNAs, increase in expression across development (supplementary Fig. 6E).

509 Together, these data reveal that NRDE-3 binds to the same group of small RNAs as CSR-1 in
510 early embryos, and may work hand-in-hand with CSR-1 to repress transcripts of maternal origin.
511 To further investigate whether NRDE-3 and CSR-1 function synergistically, we examined
512 the fertility of the *csr-1::degron* strain and the *csr-1::degron*; *gfp::nrde-3(HK-AA)* strain upon auxin
513 treatment to deplete CSR-1. As expected, both strains had 100% viable progeny with ethanol
514 control treatment (supplementary Fig. 6F). When growing on 4mM auxin plates, the number of
515 embryos laid by the *csr-1::degron*; *gfp::nrde-3(HK-AA)* double mutant was significantly lower
516 compared to the *csr-1::degron* single mutant and more of the double mutant produced no embryos
517 (11.9%) compared to the *csr-1::degron* single mutant strain (7.5%), indicating a more severe
518 sterility defect in the *csr-1::degron; nrde-3(HK-AA)* double mutant compared to the *csr-1::degron*
519 alone (Fig. 6F, supplementary Fig. 6F). Additionally, 5.9% of the auxin-treated *csr-1::degron*
520 animals produced some F1 progeny that hatched, compared to no F1 hatching for any of the
521 auxin-treated *csr-1::degron; gfp::nrde-3(HK-AA)* double mutant animals (supplementary Fig. 6F).
522 All together, these results indicate that loss of NRDE-3 enhances the fertility defects of CSR-1
523 and suggest that NRDE-3 and CSR-1 function synergistically for early embryonic development.
524 NRDE-3 is a nuclear Argonaute protein that recruits histone methyltransferases to target
525 genes to deposit histone modifications such as H3K9me3 and H3K27me3 at these loci (Guang
526 et al. 2008; Burton et al. 2011; Mao et al. 2015). To examine whether NRDE-3 promotes
527 deposition of H3K9me3 at CSR-target genes during embryogenesis, we analyzed the published
528 anti-H3K9me3 ChIP-seq data of wild-type and *nrde-3* mutant mixed-staged embryos (Padeken et
529 al. 2021). In wild-type embryos, the targets of NRDE-3 in young adults, which correspond to
530 ERGO-target genes, have high H3K9me3 levels, and are significantly decreased in the *nrde-3*
531 mutant (Fig. 6G). These data are consistent with previous research demonstrating that NRDE-3
532 deposits H3K9me3 at ERGO target genes (Burton et al. 2011). However, NRDE-3 targets in early
533 embryos do not show H3K9me3 enrichment in wild-type and do not have a significant change in
534 the *nrde-3* mutant (Fig. 6G). The same trend is also observed in the early degraded and late
535 degraded targets (Fig. 6G). These results indicate that the CSR targets are not H3K9
536 trimethylated in the early embryos. However, we cannot rule out the possibility that NRDE-3 may
537 function to deposit other histone modification targets such as H3K27me3 or inhibit RNA pol II on
538 CSR targets to transcriptionally silence these genes in early embryos.
539
540 **Discussion**
541 Germ granules are phase-separated condensates that localize to the perinuclear region
542 of germ cells. In *C. elegans*, the known constituents of the germ granule have expanded over the

543 last decades, such that germ granules now comprise multiple domains including P granules,
544 *Mutator* foci, Z granules, and SIMR foci. Here we discovered that several components of SIMR
545 foci and *Mutator* foci also localize to cytoplasmic granules during specific stages of
546 embryogenesis. We propose that these granules serve as sites for the synthesis and loading of
547 22G-RNAs into the nuclear Argonaute NRDE-3. Furthermore, we showed that NRDE-3 switches
548 its small RNA targets during embryogenesis, coincident with the formation of SIMR granules.
549 Together, our study reveals a new world of embryonic RNAi factor condensates and uncovers
550 two temporally distinct roles for NRDE-3, underscoring the need for careful examination of
551 localization and targets of RNAi pathways across development (Fig. 7A).
552

553 **A role for SIMR-1 as a platform for nuclear Argonaute protein loading**

554 Previously we demonstrated that SIMR-1 and HRDE-2 are required to recruit unloaded
555 HRDE-1, the germline nuclear Argonaute protein, to germ granules and to ensure correct 22G-
556 RNA loading (Chen and Phillips 2024). Here we reveal that SIMR-1 and another HRDE-2 paralog,
557 ENRI-2, are similarly essential to recruit unloaded NRDE-3, the somatic nuclear Argonaute
558 protein, to embryonic SIMR granules. We speculate that SIMR-1 and ENRI-2 are similarly
559 important for NRDE-3 22G-RNA loading; however, we did not observe a significant change in the
560 small RNAs loaded by NRDE-3 in *simr-1* or *enri-2* mutant embryos. While initially surprising based
561 on the results of similar experiments with HRDE-1 in the germline, we envision several possible
562 explanations. First, it is possible that SIMR-1 and ENRI-2 act to bring unloaded NRDE-3 in close
563 proximity to the ERGO-dependent 22G-RNA biogenesis machinery, but that NRDE-3 loading can
564 still occur diffusely in the cytoplasm, albeit with lower efficiency. In addition, both the RdRP RRF-
565 1 and unloaded NRDE-3 diffusely localize to cytoplasm in the *simr-1* mutant (Fig. 3A, 4C),
566 suggesting that NRDE-3 may load the ERGO-class small RNAs synthesized in the cytoplasm in
567 the absence of SIMR-1. Differences in NRDE-3 loading efficiency would likely not be detected by
568 our NRDE-3 IP-small RNA sequencing experiment. Second, SIMR-1 and ENRI-2 could act to
569 sequester unloaded NRDE-3 away from other small RNAs (i.e. CSR-class 22G-RNAs) to prevent
570 misloading. Misloading should be detectable in our NRDE-3 IP-small RNA sequencing
571 experiment; however, it is unclear the extent to which newly synthesized, and unloaded CSR-
572 class 22G-RNAs are even present in the cytoplasm, as the primary source for CSR-class 22G-
573 RNAs may be the maternal germline. Thus, unlike in the adult germline where HRDE-1 incorrectly
574 loads CSR-class 22G-RNAs in the absence of HRDE-2, there may not be an equivalent source
575 of incorrect small RNAs that NRDE-3 can bind to (i.e. correct length, 5' nucleotide and
576 modifications) in the embryo. To further probe these possibilities, we need to more carefully

assess the dynamics of NRDE-3 loading across embryonic development and possibly disrupt the formation of embryonic CSR granules to determine whether compartmentalization of the CSR-class 22G-RNA pathway is also contributing to correct loading of NRDE-3 in the absence of SIMR-1 and ENRI-2.

We do not know the precise functions of SIMR-1 and ENRI-2, however we have previously proposed that SIMR-1 mediates protein-protein interactions through its extended Tudor domain (Manage et al. 2020). ENRI-2 and its paralog HRDE-2 have structural similarities to a HELICc domain, and SIMR-1, ENRI-2, and HRDE-2 have large unstructured domains (Supplementary Fig. 7A) (Lewis et al. 2020; Chen and Phillips 2024). With the advent of protein complex prediction algorithms (Abramson et al. 2024), we sought to examine the potential physical interactions between ENRI-2 and NRDE-3, as well as their paralogs HRDE-2 and HRDE-1. In both models, the structured HELICc domain of HRDE-2 and ENRI-2 dock on the Mid domain of their respective Argonaute partners. Interestingly, the unstructured C-terminal domains of ENRI-2 and HRDE-2 extend into the small RNA binding pocket of their respective nuclear Argonaute binding partners (Supplementary Fig. 7B). At this point, we do not know whether these structures are reflective of the actual geometry of the proteins *in vivo*, but it is tempting to speculate that the C-terminal disordered regions of the ENRI-2/HRDE-2 proteins could regulate 22G-RNA loading through interaction with the small RNA binding pocket of NRDE-3 and HRDE-1. Further study will be necessary to determine whether these interactions between disordered regions and the small RNA binding pocket are necessary for correct small RNA loading and whether that mechanism extends to other WAGO proteins.

Compartmentalization of RNAi pathways

Most of the studies on the organization of *C. elegans* RNAi factors in granules focus on the germline. Here we find that multiple proteins associated with 22G-RNA biogenesis and function, including SIMR-1, RDE-3, RRF-1, ENRI-2, and unloaded NRDE-3, are localized distinct condensates in *C. elegans* embryos. We speculate that these SIMR granules, which appear and then disappear during the course of embryonic development, play a functional role in the NRDE-3 nuclear RNAi pathway. This idea leads to an intriguing question: what role does organization of the RNAi pathways into condensates play in the soma vs. in the germline?

In germ cells, RNAi factors are visibly segregated into distinct compartments within the germ granule which assemble hierarchically (Uebel et al. 2023). Germ granules are also intimately linked to nuclear pores, leading to a model where highly concentrated mRNAs, newly exported from and adjacent to the nuclear pore, nucleate assembly of regulatory factors into

visible granules. In fact, nuclear pores are clustered beneath germ granules in germ cells, and evidence suggests that most, if not all, nascent mRNAs are exported through pores associated with germ granules (Pitt et al. 2000; Sheth et al. 2010). In contrast, nuclear pores are distributed more evenly across the nuclear periphery in embryos and, in this work, we find that while some embryonic SIMR granules appear adjacent to the nuclear periphery, many are distributed in the cytoplasm (see Fig. 2A, for example). Thus, unlike in germ granules, there is no obvious trajectory from the nucleus that RNAs would follow to end up in embryonic SIMR granules. Further, in the germline, we have speculated that the adjacent and hierarchical assembly of germ granule compartments could be determined by the order of molecular events required for RNA silencing (Uebel et al. 2023). While we on occasion see docking between embryonic SIMR granules and CSR granules (Fig. 4H), we do not see any more complex arrangement of granule compartments in embryos similar to what we have observed in the germline. What that means regarding the functionality of embryonic SIMR granules is unclear. Another possibility worth considering is that SIMR granules are not actually required for ERGO-dependent 22G-RNA biogenesis and NRDE-3 loading in embryos but rather that they reflect a concentration of the small RNA biogenesis machinery beyond the solubility limit of the cytoplasm, resulting in the demixing of some RNP complexes into visible SIMR granules (Putnam et al. 2023). By this “incidental condensate” model, ERGO-dependent 22G-RNA biogenesis and NRDE-3 loading occur just as efficiently, or perhaps more so, diffusely in the cytoplasm.

Both embryonic and germ granules exhibit dynamic expression patterns, suggesting that expression and function of small RNA factors are critical at discrete developmental time points. In the germline, multiple Argonaute proteins are expressed exclusively during oogenesis (ERGO-1) or spermatogenesis (ALG-3, ALG-4, CSR-1b, WAGO-10) (Billi et al. 2012; Han et al. 2009; Conine et al. 2010; Reinke et al. 2004; Nguyen and Phillips 2021; Charlesworth et al. 2021) and MUT-16 expression fluctuates across germ cell development, peaking in the mitotic region (Uebel et al. 2020). Similarly, embryonic SIMR granules appear in early embryos and disappear by late embryogenesis. Regardless as to whether SIMR granules are incidental condensates or functional sites for NRDE-3 loading, these data indicate that the levels or activities of these proteins are developmentally regulated.

It is additionally curious that embryonic and germ granules share many protein components yet possess distinct differences in content and assembly requirements. For instance, several RNAi proteins, such as RRF-1 and RDE-3, are shared between *Mutator* foci and embryonic SIMR granules, while the paralogous ENRI-2/NRDE-3 and HRDE-2/HRDE-1 pairs are found in embryonic SIMR granules and germline SIMR foci, respectively. It is unclear why the

645 *Mutator* and SIMR components are visible as separate compartments in germ granules but are
646 together in embryonic SIMR foci. This difference is highlighted by the requirement for MUT-16 in
647 the assembly of embryonic SIMR granules but not germline SIMR foci (Fig. 4D) (Manage et al.
648 2020). Further investigation into the assembly and protein components of embryonic and germ
649 granules will be crucial for elucidating the functional differences between embryonic and germ
650 granules and dissecting the mechanisms of 22G-RNA loading into NRDE-3.
651
652 **The small RNA plasticity of NRDE-3**
653 Argonautes are conventionally known to bind small RNAs with high specificity. In this
654 study, we unveil the remarkable versatility of the nuclear Argonaute NRDE-3, demonstrating its
655 ability to bind multiple classes of small RNAs and exhibit distinct functions throughout
656 development. Argonaute proteins with the capacity to bind multiple types or classes of small RNAs
657 have been observed in other organisms. For example, both siRNAs and miRNAs can be loaded
658 into the four human Argonautes (Ago1-4) and both siRNAs and miRNAs can guide Ago2-
659 dependent target cleavage (Meister et al. 2004; Liu et al. 2004). Our discovery is somewhat
660 different, however, in that NRDE-3 binds its two preferred classes of small RNAs, CSR-class 22G-
661 RNAs and ERGO-dependent 22G-RNAs, at distinct developmental stages, indicating that there
662 must be a switch from one class of small RNA to the other during embryogenesis. Interestingly,
663 a more recent study in the parasitic nematode *Acaris* revealed that the *Acaris* paralog of NRDE-
664 3, AsNRDE-3, exhibits a dramatic change in associated small RNAs during spermatogenesis,
665 targeting repetitive sequences and transposons in early stages of spermatogenesis and mRNAs
666 in late meiosis (Zagoskin et al. 2022). Curiously, the mRNAs targeted by AsNRDE-3 in late
667 meiosis largely overlap with the targets of AsCSR-1, the *Ascaris* paralog of CSR-1, and it is
668 proposed that AsNRDE-3 could act in concert with AsCSR-1 at the late stages of meiosis to clear
669 spermatogenic and meiotic mRNAs from the developing spermatids (Zagoskin et al. 2022). These
670 data further suggest that the ability of NRDE-3 to target both repetitive sequences and germline-
671 expressed genes at distinct developmental timepoints may be a conserved feature of this protein.
672 It is currently unknown how this small RNA switching is achieved. It is possible that there is an
673 active mechanism to unload the CSR-class 22G-RNAs and replace them with ERGO-dependent
674 22G-RNAs, or to degrade NRDE-3 loaded with CSR-class 22G-RNAs. However, we prefer the
675 simpler model where NRDE-3 loaded with CSR-class 22G-RNAs, initially deposited into embryo
676 from the maternal germline, are diluted out as the animal develops. Newly synthesized NRDE-3
677 in the embryo is loaded with ERGO-dependent 22G-RNAs to execute the small RNA “switch.”
678 The idea that Argonaute proteins can be utilized at distinct timepoints with different small RNA

679 partners to create multi-functionality is intriguing, especially in the vein of rapidly clearing
680 transcripts from a cell to engineer a new developmental program. Achieving higher resolution
681 small RNA-Argonaute interactions with tissue- and developmental-specific staging will be crucial
682 to fully elucidate the roles of Argonaute proteins during development in *C. elegans* and other
683 organisms.

684 In summary, this work investigating the role of SIMR granules in embryos, together with
685 our previous study of SIMR foci in the germline (Chen and Phillips 2024), has identified a new
686 mechanism for small RNA loading of nuclear Argonaute proteins in *C. elegans*. The two
687 paralogous proteins, HRDE-2 and ENRI-2, recruit unloaded nuclear Argonautes HRDE-1 and
688 NRDE-3 to small RNA production centers organized by SIMR-1, where loading can occur. These
689 small RNA loading sites are essential in the germline to promote small RNA binding specificity,
690 however they may also contribute to efficiency and specificity of small RNA loading in embryos.
691 We further discovered an intriguing repository of cytoplasmic granules during embryogenesis that
692 do not exhibit the same organization or hierarchical assembly as germ granules, highlighting the
693 importance of further investigation into the relationship between RNA silencing pathways and
694 RNA granules during embryogenesis. Lastly, we observed a striking phenomenon where the
695 NRDE-3 nuclear Argonaute protein possesses the ability to switch small RNA binding partners,
696 presumably altering mRNA targets and function, during development. Together, these findings
697 reveal that the precise regulation of small RNA pathway components through diverse
698 mechanisms, such as spatial-temporal separation and hierarchical physical interactions, is crucial
699 for accurate gene regulation and developmental transitions in *C. elegans*.

700

701 **Materials and methods**

702 ***C. elegans* stains**

703 *C. elegans* strains were maintained at 20°C on NGM plates seeded with OP50 *E. coli*
704 according to standard conditions unless otherwise stated (Brenner 1974). All strains used in this
705 project are listed in Supplementary Table 1.

706

707 **CRISPR-mediated strain construction**

708 For *nrde-3(cmp324[HK-AA])*, *enri-1(cmp328)*, *enri-2(cmp318)*, and *rde-3/mut-2(cmp337)*,
709 we used an oligo repair template and RNA guide. For *enri-1(cmp320[enri-1::mCherry::2xHA])*, we
710 used an RNA guide and PCR amplified repair template (Supplementary Table 2). For injections
711 using a single gene-specific crRNA, the injection mix included 0.25 µg/µl Cas9 protein (IDT),
712 100 ng/µl tracrRNA (IDT), 14 ng/µl dpy-10 crRNA, 42 ng/µl gene-specific crRNA, and 110 ng/µl of

713 the oligo repair template. For injections using two gene-specific crRNAs, the injection mix included
714 0.25 µg/µl Cas9 protein (IDT), 100 ng/µl tracrRNA (IDT), 14 ng/µl dpy-10 crRNA, 21 ng/µl each
715 gene-specific crRNA, and 110 ng/µl of each repair template.

716 The following strains were used for injection: *enri-2(cmp318)* and *enri-1(cmp320[enri-*
717 *1::mCherry::2xHA])* into wild-type N2 strain. *nrde-3(cmp324[HK-AA]) and enri-1(cmp328)* into
718 JMC237: *nrde-3(tor131[GFP::3xFLAG::nrde-3]) X*. *rde-3/mut-2(cmp337)* into USC1615*: ego-*
719 *1(cmp317[ego-1::degron]) I; ieSi38 [Psun-1::TIR1::mRuby::sun-1 3' UTR] IV; nrde-*
720 *3(tor131[GFP::3xFLAG::nrde-3]) X*. Following injection, F1 animals with the RoI phenotype were
721 isolated and genotyped by PCR to identify heterozygous animals with the mutations of interest,
722 then F2 animals were further singled out to identify homozygous mutant animals.
723

724 **Live imaging**

725 Live imaging of *C. elegans* embryos was performed in M9 buffer. Young embryos were
726 obtained by dissecting gravid adult *C. elegans*, and old embryos were obtained by manually
727 picking embryos laid on the NGM plate. Live imaging of *C. elegans* adult germline was performed
728 in M9 buffer containing sodium azide to prevent movement. Day-one-adult *C. elegans* were
729 obtained by manually picking L4s and leaving L4s at 20°C for about 24 hours. Imaging was
730 performed on a DeltaVision Elite microscope (GE Healthcare) using a 60x N.A. 1.42 oil-immersion
731 objective. Images were pseudocolored using Adobe Photoshop.
732

733 **Granule number quantification**

734 Granule number quantification was performed in FIJI/ImageJ2 (version 2.9.0). At least 10
735 embryos were imaged on a DeltaVision Elite microscope with 37 optical sections of a total
736 22.20µm sample thickness from the bottom of the sample. Images were deconvolved to eliminate
737 backgrounds. Z stacks were opened using the 3D object counter plugin for FIJI, and the granule
738 counting threshold for each image was manually adjusted to obtain the least background and
739 most granules.
740

741 **Western blot**

742 Synchronized adult *C. elegans* were harvested (~72 h at 20 °C after L1 arrest) and 200
743 adults were loaded per lane. Proteins were resolved on 4–12% Bis-Tris polyacrylamide gels
744 (Thermo Fisher, NW04122BOX), transferred to nitrocellulose membranes (Thermo Fisher,
745 LC2001), and probed with rat anti-HA-peroxidase 1:1000 (Roche 12013819001) or mouse anti-

actin 1:10,000 (Abcam ab3280). Secondary HRP antibodies were purchased from Thermo Fisher. Unedited western blots are provided in the Source Data File.

Small RNA library preparation and sequencing

For *C. elegans* embryo staging and collection, synchronized arrested L1s were grown on enriched peptone plates at 17°C until the young adult stage. Adult *C. elegans* stage was monitored carefully under DeltaVision microscope by live imaging. For early embryo collection (<=100-cell), adult animals were washed off from plates with H_2O and bleached as soon as the first animals had 1-4 eggs (around 68-70 hours depending on the strain and the incubator temperature). For late embryo collection (>=300-cell), adult animals were washed off from plates with H_2O and bleached when about half of the worms had 1~6 eggs (~70-72 hours depending on the strain and the incubator temperature). After bleaching, embryos were washed twice with M9 buffer, and filtered through 40µm cell strainers (Fisherbrand™ Sterile Cell Strainers, 40µm) twice to clear the residual worm body. To reach >=300-cell stage for late embryo collection, embryos were additionally incubated in M9 buffer at 20°C for 4.5 hours. Then embryos were washed once with IP buffer (50 mM Tris-Cl pH 7.5, 100 mM KCl, 2.5 mM MgCl2, 0.1% Nonidet P40 substitute) containing Protease Inhibitor (Thermo Fisher A32965). Embryos were kept on ice during washes to prevent further development. 500,000 embryos were collected for each replicate. Following washes, embryos were flash-frozen by placing tubes in a container with ethanol and dry ice. A small aliquot of embryos was examined on the Deltavision microscope to confirm the developmental stage immediately before freezing. Frozen embryos were stored at -80°C until immunoprecipitation.

For immunoprecipitation followed by small RNA sequencing in embryos, ~500,000 synchronized embryos were sonicated with Fisher Sonifier 550 with a microtip (15s on, 45s off, 10% power, total 2 minutes on time). After sonication, insoluble particulate was removed by centrifugation at 21,000g for 30 minutes. Immunoprecipitation was performed using anti-FLAG Affinity Matrix (Sigma Aldrich, A2220). NRDE-3-bound RNAs were isolated using TRIzol reagent (Thermo Fisher, 15596018), followed by chloroform extraction and isopropanol precipitation. Small RNAs (18 to 30-nt) were size selected on homemade 10% Urea-polyacrylamide gels from total RNA samples. Small RNAs were treated with 5' RNA polyphosphatase (Epicenter RP8092H) and ligated to 3' pre-adenylated adapters with Truncated T4 RNA ligase (NEB M0373L). Small RNAs were then hybridized to the reverse transcription primer, ligated to the 5' adapter with T4 RNA ligase (NEB M0204L), and reverse transcribed with Superscript III (Thermo Fisher 18080-051). Small RNA libraries were amplified using Q5 High-Fidelity DNA polymerase (NEB M0491L)

780 and size selected on a homemade 10% polyacrylamide gel. Library concentration was determined
781 using the Qubit 1X dsDNA HS Assay kit (Thermo Fisher Q33231) and quality was assessed using
782 the Agilent BioAnalyzer. Libraries were sequenced on the Illumina NextSeq2000 (SE 75-bp reads)
783 platform. Primer sequences are available in Supplementary Table2. Differentially expressed gene
784 lists and gene lists used in this paper can be found in Supplementary Table3. Sequencing library
785 statistics summary can be found in Supplementary Table4.
786
787 **Bioinformatic analysis**
788 For small RNA libraries, sequences were parsed from adapters and quality filtered using FASTX-
789 Toolkit (version 0.0.13) (Greg Hannon 2010). Filtered reads were mapped to the *C. elegans*
790 genome, WS258, using Bowtie2 (version 2.5.0) (Langmead and Salzberg 2012). Mapped reads
791 were assigned to genomic features using featureCounts which is part of the Subread package
792 (version 2.0.1) (Liao et al. 2014). Differential expression analysis was performed using edgeR
793 (3.40.2) (Robinson et al. 2010). To define gene lists from IP experiments, a twofold-change cutoff,
794 an edgeR adjusted p-value of ≤0.05, and at least 10 RPM in the IP libraries were required to
795 identify genes with significant changes in small RNA levels.
796
797 **Data Availability**
798 The RNA sequencing data generated in this study are available through Gene Expression
799 Omnibus (GEO) under accession code GSE273239. Source data file is provided with this paper.
800
801 **Acknowledgements**
802 We thank the members of the Phillips lab for helpful discussions and feedback on the manuscript,
803 and the labs of Julie Claycomb, John Kim, Heng-Chi Lee, and Mihail Sarov for generously
804 providing strains. This work was supported by the National Institute of Health grant R35
805 GM119656 (to CMP). Some strains were provided by the CGC, which is funded by NIH Office of
806 Research Infrastructure Programs (P40 OD010440). Next generation sequencing was performed
807 by the USC Molecular Genomics Core, which is supported by award number P30 CA014089 from
808 the National Cancer Institute.
809
810 **Author contributions**
811 S.C.: Conceptualization, Investigation, Formal analysis, Writing–original draft, Writing–reviewing
812 and editing, Visualization

C.M.P.: Conceptualization, Formal Analysis, Writing–original draft, Writing–reviewing and editing, Supervision, Funding Acquisition.

Competing interests

The authors declare no competing interests.

Reference

Abramson J, Adler J, Dunger J, Evans R, Green T, Pritzel A, Ronneberger O, Willmore L, Ballard AJ, Bambrick J, et al. 2024. Accurate structure prediction of biomolecular interactions with AlphaFold 3. *Nature* **630**: 493–500.

Aoki K, Moriguchi H, Yoshioka T, Okawa K, Tabara H. 2007. In vitro analyses of the production and activity of secondary small interfering RNAs in C. elegans. *EMBO J* **26**: 5007–5019.

Ashe A, Bélicard T, Le Pen J, Sarkies P, Frézal L, Lehrbach NJ, Félix M-A, Miska EA. 2013. A deletion polymorphism in the Caenorhabditis elegans RIG-I homolog disables viral RNA dicing and antiviral immunity ed. D. Weigel. *eLife* **2**: e00994.

Billi AC, Alessi AF, Khivansara V, Han T, Freeberg M, Mitani S, Kim JK. 2012. The Caenorhabditis elegans HEN1 Ortholog, HENN-1, Methylates and Stabilizes Select Subclasses of Germline Small RNAs. *PLOS Genet* **8**: e1002617.

Brangwynne CP, Eckmann CR, Courson DS, Rybarska A, Hoege C, Gharakhani J, Jülicher F, Hyman AA. 2009. Germline P Granules Are Liquid Droplets That Localize by Controlled Dissolution/Condensation. *Science* **324**: 1729–1732.

Brenner S. 1974. THE GENETICS OF CAENORHABDITIS ELEGANS. *Genetics* **77**: 71–94.

Buck AH, Blaxter M. 2013. Functional diversification of Argonautes in nematodes: an expanding universe. *Biochem Soc Trans* **41**: 881–886.

Buckley BA, Burkhart KB, Gu SG, Spracklin G, Kershner A, Fritz H, Kimble J, Fire A, Kennedy S. 2012. A nuclear Argonaute promotes multigenerational epigenetic inheritance and germline immortality. *Nature* **489**: 447–451.

Burton NO, Burkhart KB, Kennedy S. 2011. Nuclear RNAi maintains heritable gene silencing in Caenorhabditis elegans. *Proc Natl Acad Sci* **108**: 19683–19688.

Charlesworth AG, Seroussi U, Lehrbach NJ, Renaud MS, Sundby AE, Molnar RI, Lao RX, Willis AR, Woock JR, Aber MJ, et al. 2021. Two isoforms of the essential C. elegans Argonaute CSR-1 differentially regulate sperm and oocyte fertility. *Nucleic Acids Res* **49**: 8836–8865.

Chen C-CG, Simard MJ, Tabara H, Brownell DR, McCollough JA, Mello CC. 2005. A Member of the Polymerase β Nucleotidyltransferase Superfamily Is Required for RNA Interference in C. elegans. *Curr Biol* **15**: 378–383.

849 Chen S, Phillips CM. 2024. HRDE-2 drives small RNA specificity for the nuclear Argonaute
850 protein HRDE-1. *Nat Commun* **15**: 957.

851 Claycomb JM, Batista PJ, Pang KM, Gu W, Vasale JJ, Wolfswinkel JC van, Chaves DA,
852 Shirayama M, Mitani S, Ketting RF, et al. 2009. The Argonaute CSR-1 and Its 22G-RNA
853 Cofactors Are Required for Holocentric Chromosome Segregation. *Cell* **139**: 123–134.

854 Conine CC, Batista PJ, Gu W, Claycomb JM, Chaves DA, Shirayama M, Mello CC. 2010.
855 Argonautes ALG-3 and ALG-4 are required for spermatogenesis-specific 26G-RNAs and
856 thermotolerant sperm in Caenorhabditis elegans. *Proc Natl Acad Sci* **107**: 3588–3593.

857 Ding S-W, Li H, Lu R, Li F, Li W-X. 2004. RNA silencing: a conserved antiviral immunity of
858 plants and animals. *Virus Res* **102**: 109–115.

859 Du Z, Shi K, Brown JS, He T, Wu W-S, Zhang Y, Lee H-C, Zhang D. 2023. Condensate
860 cooperativity underlies transgenerational gene silencing. *Cell Rep* **42**.
861 https://www.cell.com/cell-reports/abstract/S2211-1247(23)00870-7 (Accessed May 16,
862 2024).

863 Félix M-A, Ashe A, Piffaretti J, Wu G, Nuez I, Bélicard T, Jiang Y, Zhao G, Franz CJ, Goldstein
864 LD, et al. 2011. Natural and Experimental Infection of Caenorhabditis Nematodes by
865 Novel Viruses Related to Nodaviruses. *PLOS Biol* **9**: e1000586.

866 Fire A, Xu S, Montgomery MK, Kostas SA, Driver SE, Mello CC. 1998. Potent and specific
867 genetic interference by double-stranded RNA in Caenorhabditis elegans. *Nature* **391**:
868 806–811.

869 Fischer SEJ, Montgomery TA, Zhang C, Fahlgren N, Breen PC, Hwang A, Sullivan CM,
870 Carrington JC, Ruvkun G. 2011. The ERI-6/7 Helicase Acts at the First Stage of an
871 siRNA Amplification Pathway That Targets Recent Gene Duplications. *PLOS Genet* **7**:
872 e1002369.

873 Gallo CM, Munro E, Rasoloson D, Merritt C, Seydoux G. 2008. Processing bodies and germ
874 granules are distinct RNA granules that interact in *C. elegans* embryos. *Dev Biol* **323**:
875 76–87.

876 Gent JI, Lamm AT, Pavelec DM, Maniar JM, Parameswaran P, Tao L, Kennedy S, Fire AZ.
877 2010. Distinct Phases of siRNA Synthesis in an Endogenous RNAi Pathway in C.
878 elegans Soma. *Mol Cell* **37**: 679–689.

879 Greg Hannon. 2010. FASTX-Toolkit: FASTQ/a short-reads pre-processing tools.
880 http://hannonlab.cshl.edu/fastx_toolkit/.

881 Gu W, Shirayama M, Conte D, Vasale J, Batista PJ, Claycomb JM, Moresco JJ, Youngman EM,
882 Keys J, Stoltz MJ, et al. 2009. Distinct Argonaute-Mediated 22G-RNA Pathways Direct
883 Genome Surveillance in the C. elegans Germline. *Mol Cell* **36**: 231–244.

884 Guang S, Bochner AF, Pavelec DM, Burkhart KB, Harding S, Lachowiec J, Kennedy S. 2008.
885 An Argonaute Transports siRNAs from the Cytoplasm to the Nucleus. *Science* **321**: 537–
886 541.

887 Han T, Manoharan AP, Harkins TT, Bouffard P, Fitzpatrick C, Chu DS, Thierry-Mieg D, Thierry-
888 Mieg J, Kim JK. 2009. 26G endo-siRNAs regulate spermatogenic and zygotic gene
889 expression in Caenorhabditis elegans. *Proc Natl Acad Sci* **106**: 18674–18679.

890 Han W, Sundaram P, Kenjale H, Grantham J, Timmons L. 2008. The Caenorhabditis elegans
891 rsd-2 and rsd-6 Genes Are Required for Chromosome Functions During Exposure to
892 Unfavorable Environments. *Genetics* **178**: 1875–1893.

893 Höck J, Meister G. 2008. The Argonaute protein family. *Genome Biol* **9**: 210.

894 Ishidate T, Ozturk AR, Durning DJ, Sharma R, Shen E, Chen H, Seth M, Shirayama M, Mello
895 CC. 2018. ZNFX-1 Functions within Perinuclear Nuage to Balance Epigenetic Signals.
896 *Mol Cell* **70**: 639-649.e6.

897 Langmead B, Salzberg SL. 2012. Fast gapped-read alignment with Bowtie 2. *Nat Methods* **9**:
898 357–359.

899 Lewis A, Berkyurek AC, Greiner A, Sawh AN, Vashisht A, Merrett S, Flamand MN,
900 Wohlschlegel J, Sarov M, Miska EA, et al. 2020. A Family of Argonaute-Interacting
901 Proteins Gates Nuclear RNAi. *Mol Cell* **78**: 862-875.e8.

902 Liao Y, Smyth GK, Shi W. 2014. featureCounts: an efficient general purpose program for
903 assigning sequence reads to genomic features. *Bioinformatics* **30**: 923–930.

904 Liu J, Carmell MA, Rivas FV, Marsden CG, Thomson JM, Song J-J, Hammond SM, Joshua-Tor
905 L, Hannon GJ. 2004. Argonaute2 Is the Catalytic Engine of Mammalian RNAi. *Science*
906 **305**: 1437–1441.

907 Ma J-B, Yuan Y-R, Meister G, Pei Y, Tuschl T, Patel DJ. 2005. Structural basis for 5′-end-
908 specific recognition of guide RNA by the A. fulgidus Piwi protein. *Nature* **434**: 666–670.

909 Manage KI, Rogers AK, Wallis DC, Uebel CJ, Anderson DC, Nguyen DAH, Arca K, Brown KC,
910 Cordeiro Rodrigues RJ, de Albuquerque BF, et al. 2020. A tudor domain protein, SIMR-
911 1, promotes siRNA production at piRNA-targeted mRNAs in C. elegans eds. O. Hobert
912 and J.L. Manley. *eLife* **9**: e56731.

913 Mao H, Zhu C, Zong D, Weng C, Yang X, Huang H, Liu D, Feng X, Guang S. 2015. The Nrde
914 Pathway Mediates Small-RNA-Directed Histone H3 Lysine 27 Trimethylation in
915 Caenorhabditis elegans. *Curr Biol* **25**: 2398–2403.

916 McEwan DL, Weisman AS, Hunter CP. 2012. Uptake of Extracellular Double-Stranded RNA by
917 SID-2. *Mol Cell* **47**: 746–754.

918 Meister G, Landthaler M, Patkaniowska A, Dorsett Y, Teng G, Tuschl T. 2004. Human
919 Argonaute2 Mediates RNA Cleavage Targeted by miRNAs and siRNAs. *Mol Cell* **15**:
920 185–197.

921 Nguyen DAH, Phillips CM. 2021. Arginine methylation promotes siRNA-binding specificity for a
922 spermatogenesis-specific isoform of the Argonaute protein CSR-1. *Nat Commun* **12**:
923 4212.

924 Ouyang JPT, Folkmann A, Bernard L, Lee C-Y, Seroussi U, Charlesworth AG, Claycomb JM,
925 Seydoux G. 2019. P Granules Protect RNA Interference Genes from Silencing by
926 piRNAs. *Dev Cell* **50**: 716-728.e6.

927 Padeken J, Methot S, Zeller P, Delaney CE, Kalck V, Gasser SM. 2021. Argonaute NRDE-3
928 and MBT domain protein LIN-61 redundantly recruit an H3K9me3 HMT to prevent
929 embryonic lethality and transposon expression. *Genes Dev* **35**: 82–101.

930 Pak J, Fire A. 2007. Distinct Populations of Primary and Secondary Effectors During RNAi in C.
931 elegans. *Science* **315**: 241–244.

932 Parker R, Sheth U. 2007. P Bodies and the Control of mRNA Translation and Degradation. *Mol*
933 *Cell* **25**: 635–646.

934 Phillips CM, Montgomery BE, Breen PC, Roovers EF, Rim Y-S, Ohsumi TK, Newman MA, van
935 Wolfswinkel JC, Ketting RF, Ruvkun G, et al. 2014. MUT-14 and SMUT-1 DEAD Box
936 RNA Helicases Have Overlapping Roles in Germline RNAi and Endogenous siRNA
937 Formation. *Curr Biol* **24**: 839–844.

938 Phillips CM, Montgomery TA, Breen PC, Ruvkun G. 2012. MUT-16 promotes formation of
939 perinuclear Mutator foci required for RNA silencing in the C. elegans germline. *Genes*
940 *Dev* **26**: 1433–1444.

941 Pitt JN, Schisa JA, Priess JR. 2000. P Granules in the Germ Cells of *Caenorhabditis elegans*
942 Adults Are Associated with Clusters of Nuclear Pores and Contain RNA. *Dev Biol* **219**:
943 315–333.

944 Putnam A, Thomas L, Seydoux G. 2023. RNA granules: functional compartments or incidental
945 condensates? *Genes Dev* **37**: 354–376.

946 Quarato P, Singh M, Cornes E, Li B, Bourdon L, Mueller F, Didier C, Cecere G. 2021. Germline
947 inherited small RNAs facilitate the clearance of untranslated maternal mRNAs in C.
948 elegans embryos. *Nat Commun* **12**: 1441.

949 Reinke V, Gil IS, Ward S, Kazmer K. 2004. Genome-wide germline-enriched and sex-biased
950 expression profiles in Caenorhabditis elegans. *Development* **131**: 311–323.

951 Robinson MD, McCarthy DJ, Smyth GK. 2010. edgeR: a Bioconductor package for differential
952 expression analysis of digital gene expression data. *Bioinformatics* **26**: 139–140.

953 Sakaguchi A, Sarkies P, Simon M, Doebley A-L, Goldstein LD, Hedges A, Ikegami K, Alvares
954 SM, Yang L, LaRocque JR, et al. 2014. Caenorhabditis elegans RSD-2 and RSD-6
955 promote germ cell immortality by maintaining small interfering RNA populations. *Proc*
956 *Natl Acad Sci* **111**: E4323–E4331.

957 Sarkies P, Miska EA. 2013. RNAi pathways in the recognition of foreign RNA: antiviral
958 responses and host–parasite interactions in nematodes. *Biochem Soc Trans* **41**: 876–
959 880.

960 Seroussi U, Li C, Sundby AE, Lee TL, Claycomb JM, Saltzman AL. 2022. Mechanisms of
961 epigenetic regulation by C. elegans nuclear RNA interference pathways. *Semin Cell Dev*
962 *Biol* **127**: 142–154.

963 Seroussi U, Lugowski A, Wadi L, Lao RX, Willis AR, Zhao W, Sundby AE, Charlesworth AG,
964 Reinke AW, Claycomb JM. 2023. A comprehensive survey of C. elegans argonaute
965 proteins reveals organism-wide gene regulatory networks and functions eds. D.E.
966 James, A. Pasquenelli, and S. Kennedy. *eLife* **12**: e83853.

967 Seydoux G, Dunn MA. 1997. Transcriptionally repressed germ cells lack a subpopulation of
968 phosphorylated RNA polymerase II in early embryos of Caenorhabditis elegans and
969 Drosophila melanogaster. *Development* **124**: 2191–2201.

970 Seydoux G, Fire A. 1994. Soma-germline asymmetry in the distributions of embryonic RNAs in
971 Caenorhabditis elegans. *Development* **120**: 2823–2834.

972 Sheth U, Pitt J, Dennis S, Priess JR. 2010. Perinuclear P granules are the principal sites of
973 mRNA export in adult C. elegans germ cells. *Development* **137**: 1305–1314.

974 Shirayama M, Stanney W, Gu W, Seth M, Mello CC. 2014. The Vasa Homolog RDE-12
975 Engages Target mRNA and Multiple Argonaute Proteins to Promote RNAi in C. elegans.
976 *Curr Biol* **24**: 845–851.

977 Shukla A, Yan J, Pagano DJ, Dodson AE, Fei Y, Gorham J, Seidman JG, Wickens M, Kennedy
978 S. 2020. poly(UG)-tailed RNAs in genome protection and epigenetic inheritance. *Nature*
979 **582**: 283–288.

980 Sijen T, Fleenor J, Simmer F, Thijssen KL, Parrish S, Timmons L, Plasterk RHA, Fire A. 2001.
981 On the Role of RNA Amplification in dsRNA-Triggered Gene Silencing. *Cell* **107**: 465–
982 476.

983 Singh M, Cornes E, Li B, Quarato P, Bourdon L, Dingli F, Loew D, Proccacia S, Cecere G.
984 2021. Translation and codon usage regulate Argonaute slicer activity to trigger small
985 RNA biogenesis. *Nat Commun* **12**: 3492.

986 Spracklin G, Fields B, Wan G, Becker D, Wallig A, Shukla A, Kennedy S. 2017. The RNAi
987 Inheritance Machinery of Caenorhabditis elegans. *Genetics* **206**: 1403–1416.

988 Tijsterman M, May RC, Simmer F, Okihara KL, Plasterk RHA. 2004. Genes Required for
989 Systemic RNA Interference in Caenorhabditis elegans. *Curr Biol* **14**: 111–116.

990 Uebel CJ, Agbede D, Wallis DC, Phillips CM. 2020. Mutator Foci Are Regulated by
991 Developmental Stage, RNA, and the Germline Cell Cycle in Caenorhabditis elegans. *G3*
992 *GenesGenomesGenetics* **10**: 3719–3728.

993 Uebel CJ, Manage KI, Phillips CM. 2021. SIMR foci are found in the progenitor germ cells of C.
994 elegans embryos. *MicroPublication Biol*.
995 https://www.micropublication.org/journals/biology/micropub-biology-000374 (Accessed
996 May 16, 2024).

997 Uebel CJ, Rajeev S, Phillips CM. 2023. Caenorhabditis elegans germ granules are present in
998 distinct configurations and assemble in a hierarchical manner. *Dev Camb Engl* **150**.
999 http://eutils.ncbi.nlm.nih.gov/entrez/eutils/elink.fcgi?dbfrom=pubmed&id=38009921&retm
1000 ode=ref&cmd=prlinks.

1001 Updike D, Strome S. 2010. P Granule Assembly and Function in Caenorhabditis elegans Germ
1002 Cells. *J Androl* **31**: 53–60.

1003 Vasale JJ, Gu W, Thivierge C, Batista PJ, Claycomb JM, Youngman EM, Duchaine TF, Mello
1004 CC, Conte D. 2010. Sequential rounds of RNA-dependent RNA transcription drive
1005 endogenous small-RNA biogenesis in the ERGO-1/Argonaute pathway. *Proc Natl Acad*
1006 *Sci* **107**: 3582–3587.

1007 Wan G, Fields BD, Spracklin G, Shukla A, Phillips CM, Kennedy S. 2018. Spatiotemporal
1008 regulation of liquid-like condensates in epigenetic inheritance. *Nature* **557**: 679–683.

1009 Wang JT, Seydoux G. 2013. Germ Cell Specification. In *Germ Cell Development in C. elegans*
1010 (ed. T. Schedl), *Advances in Experimental Medicine and Biology*, pp. 17–39, Springer,
1011 New York, NY https://doi.org/10.1007/978-1-4614-4015-4_2 (Accessed November 15,
1012 2023).

1013 Winston WM, Sutherlin M, Wright AJ, Feinberg EH, Hunter CP. 2007. Caenorhabditis elegans
1014 SID-2 is required for environmental RNA interference. *Proc Natl Acad Sci* **104**: 10565–
1015 10570.

1016 Yang H, Vallandingham J, Shiu P, Li H, Hunter CP, Mak HY. 2014. The DEAD Box Helicase
1017 RDE-12 Promotes Amplification of RNAi in Cytoplasmic Foci in C. elegans. *Curr Biol* **24**:
1018 832–838.

1019 Yigit E, Batista PJ, Bei Y, Pang KM, Chen C-CG, Tolia NH, Joshua-Tor L, Mitani S, Simard MJ,
1020 Mello CC. 2006. Analysis of the C. elegans Argonaute Family Reveals that Distinct
1021 Argonautes Act Sequentially during RNAi. *Cell* **127**: 747–757.

1022 Zagoskin MV, Wang J, Neff AT, Veronezi GMB, Davis RE. 2022. Small RNA pathways in the
1023 nematode Ascaris in the absence of piRNAs. *Nat Commun* **13**: 837.

1024 Zhang C, Montgomery TA, Fischer SEJ, Garcia SMDA, Riedel CG, Fahlgren N, Sullivan CM,
1025 Carrington JC, Ruvkun G. 2012. The Caenorhabditis elegans RDE-10/RDE-11 Complex
1026 Regulates RNAi by Promoting Secondary siRNA Amplification. *Curr Biol* **22**: 881–890.

1027 Zhang L, Ward JD, Cheng Z, Dernburg AF. 2015. The auxin-inducible degradation (AID) system
1028 enables versatile conditional protein depletion in C. elegans. *Development* **142**: 4374–
1029 4384.

1030

1031 **Figure Legends**

1032 **Figure 1. SIMR-1 and ENRI-2 colocalize at somatic granules in embryos.**

1033 A. Summary of IP-mass spectrometry interactions detected between NRDE-3, ENRI-2,
1034 ENRI-1, and SIMR-1 from previously published studies (Chen and Phillips, 2024, Lewis
1035 *et al.*, 2021). The number of replicates from which the interaction was detected relative
1036 to the total number of replicates performed is indicated.

1037 B. Live imaging of GFP::3xFLAG::NRDE-3 and SIMR-1::mCherry::2xHA; ENRI-
1038 2::2xTy1::GFP embryos at different stages (4-cell, 8-cell, 28-cell, 100-cell, 200-cell, and
1039 comma). Boxes identify the location of Z_2 and Z_3 primordial germ cells, showing that
1040 SIMR-1 is present in germ granules while ENRI-2 is not. At least five individual embryos
1041 were imaged for each genotype and stage. Scale bars, 5 µm.

1042 C. Box plot of SIMR-1::mCherry::2xHA granule number quantification at different embryonic
1043 stages (4-cell, 8-cell, 28-cell, 100-cell, and 200-cell). At least ten individual embryos at
1044 each stage were used for quantification. Each dot represents an individual embryo, and
1045 all data points are shown. Bolded midline indicates median value, box indicates the first
1046 and third quartiles, and whiskers represent the most extreme data points within 1.5 times
1047 the interquartile range. Lines connect the mean granule number for each stage, illustrating
1048 the change in number of SIMR-1 granules across the developmental stages of the embryo.
1049 Two-tailed t-tests were performed to determine statistical significance and p-values were
1050 adjusted for multiple comparisons. See Materials and Methods for a detailed description
1051 of quantification methods.

1052

1053 **Figure 2. Unloaded NRDE-3 localizes to cytoplasmic granules with SIMR-1.**

1054 A. Live imaging of GFP::3xFLAG::NRDE-3 embryos in *eri-1*, *rde-3*, and *nrde-3(HK-AA)*
1055 mutants at 8-cell, 100-cell, and comma stage embryos. At least five individual embryos
1056 were imaged for each genotype and stage. Arrows point to granule localization of
1057 NRDE-3 in the 100-cell stage. Asterisks highlights the localization of NRDE-3 to the
1058 nucleus of the Z2 and Z3 primordial germ cells. Scale bars, 5 µm.

1059 B. Box plot of GFP::3xFLAG::NRDE-3 granule number quantification in different mutants.

1060 C. Box plot of GFP::3xFLAG::NRDE-3(HK-AA) granule number quantification at different
1061 embryonic stages. Lines connect the mean granule number (red dots) for each stage,
1062 illustrating the change in change in number of NRDE-3 granules across embryonic
1063 development.

1064 D. Live imaging of SIMR-1::mCherry::2xHA; GFP::3xFLAG::NRDE-3(HK-AA) at 100-cell
1065 stage. Arrows point to examples of colocalization between SIMR-1 and NRDE-3(HK-AA).
1066 At least ten individual embryos were imaged. Scale bars, 5 μm.
1067 For box plots in B and C, at least twelve individual embryos in each mutant were used for
1068 quantification. Each dot represents an individual embryo, and all data points are shown.
1069 Bolded midline indicates median value, box indicates the first and third quartiles, and
1070 whiskers represent the most extreme data points within 1.5 times the interquartile range.
1071 Two-tailed t-tests were performed to determine statistical significance and p-values were
1072 adjusted for multiple comparisons. See Materials and Methods for a detailed description
1073 of quantification methods.
1074
1075 **Figure 3. SIMR-1 recruits ENRI-2 and then NRDE-3 to cytoplasmic granules.**
1076 A. Live imaging of GFP::3xFLAG::NRDE-3(HK-AA) embryos in *simr-1* and *enri-2* mutants,
1077 and GFP::3xFLAG::NRDE-3 embryos in a *simr-1; eri-1* double mutant at 8-cell, 100-cell,
1078 and comma stages. Asterisk marks the nuclear localization of NRDE-3 visible in a
1079 primordial germ cell. At least five individual embryos were imaged for each genotype and
1080 stage. Scale bars, 5 μm.
1081 B. Live imaging of ENRI-2::2xTy1::GFP embryos in a *simr-1* mutant and SIMR-
1082 1::GFP::3xFLAG embryos in an *enri-2* mutant. At least five individual embryos were
1083 imaged for each genotype and stage. Arrows point to examples of cytoplasmic SIMR-1
1084 granules still visible in the *enri-2* mutant. Box surrounds a primordial germ cell displaying
1085 germ granule localization of SIMR-1. Scale bars, 5 μm.
1086
1087 **Figure 4. CSR and WAGO pathway proteins localize to distinct cytoplasmic granules.**
1088 A. Live imaging of SIMR-1::mCherry::2xHA; RDE-3::GFP embryo at 100-cell stage,
1089 showing that RDE-3 colocalizes with SIMR-1. At least five individual embryos were
1090 imaged for each genotype and stage. Arrowheads point to examples of colocalization
1091 between SIMR-1 and RDE-3 at cytoplasmic granules. Scale bars, 5 μm.
1092 B. Live imaging of SIMR-1::GFP::3xFLAG; HA::EGO-1::mCherry::RRF-1 at 100-cell stage
1093 embryo, showing that RRF-1 colocalizes with SIMR-1. At least five individual embryos
1094 were imaged for each genotype and stage. Arrowheads point to examples of
1095 colocalization between SIMR-1 and RRF-1 at cytoplasmic granules. Scale bars, 5 μm.
1096 C. Live imaging of mCherry::EGO-1::GFP::RRF-1 in a *simr-1* mutant, showing that RRF-1
1097 no longer associates with cytoplasmic granules, while EGO-1 remains associated with

1098 granules in the *simr-1* mutant. At least five individual embryos were imaged. Arrowheads
1099 point to examples of cytoplasmic EGO-1 granules in a *simr-1* mutant. Scale bars, 5 µm.
1100 D. Live imaging of SIMR-1::mCherry::2xHA embryos in a *mut-16* mutant at 8-cell, 100-cell,
1101 and comma stages. At least five individual embryos were imaged. Asterisks indicate
1102 spindle localization of SIMR-1 in a *mut-16* mutant. Box highlights germ granule
1103 localization of SIMR-1 in a comma-stage, *mut-16* mutant embryo. Scale bars, 5 µm.
1104 E. Live imaging of GFP::3xFLAG::CSR-1 embryos at different stages (4-cell, 28-cell, 100-
1105 cell, 200-cell, and comma), shows that CSR-1 localizes to cytoplasmic granules in early
1106 embryos and is restricted to germ granules in late embryos. At least three individual
1107 embryos were imaged for each stage. Dotted white line marks perimeter of the embryo.
1108 Box marks germ granule localization of CSR-1. Scale bars, 5 µM.
1109 F. Box plot quantifying GFP::3xFLAG::CSR-1 granules at different embryonic stages. At least
1110 ten embryos at each stage were used for quantification. Each dot represents an individual
1111 embryo, and all data points are shown. Bolded midline indicates median value, box
1112 indicates the first and third quartiles, and whiskers represent the most extreme data points
1113 within 1.5 times the interquartile range. Lines connect the mean granule number (red dots)
1114 at each stage, illustrating the change in number of CSR-1 granules across embryonic
1115 development. Two-tailed t-tests were performed to determine statistical significance and
1116 p-values were adjusted for multiple comparisons. See Materials and Methods for a
1117 detailed description of quantification methods.
1118 G. Live imaging of mCherry::EGO-1; GFP::3xFLAG::::CSR-1 embryo at 28-cell stage,
1119 showing CSR-1 colocalization with EGO-1. At least ten individual embryos were imaged.
1120 Arrowheads point to examples of CSR-1 and EGO-1 colocalization at cytoplasmic
1121 granules. Scale bars, 5 µm.
1122 H. Live imaging of SIMR-1::mCherry::2xHA; GFP::3xFLAG::CSR-1 embryo at 28-cell stage,
1123 showing the absence of colocalization between SIMR-1 and CSR-1 with occasional
1124 adjacent localization. At least ten individual embryos were imaged. Arrowheads point to
1125 examples of SIMR-1 and CSR-1 granules that do not colocalize. Insets display examples
1126 of SIMR-1 and CSR-1 granules that are found adjacent to each other. Dotted white line
1127 marks perimeter of embryo. Scale bars, 5 µm.
1128 I. Model of CSR and SIMR granules in the somatic cells of *C. elegans* embryos. The
1129 RdRP EGO-1, which synthesizes CSR-class 22G-RNAs, localizes to CSR granules,
1130 where CSR-1 loading may take place. The RdRP RRF-1, along with RDE-3, ENRI-2,
1131 and unloaded NRDE-3 localize to SIMR granules. SIMR-1 and ENRI-2 recruits unloaded

1132 NRDE-3 to granule where RRF-1 may synthesize ERGO-dependent 22G-RNAs for
1133 loading into NRDE-3. After loading, NRDE-3 translocates to the nucleus and silences
1134 genes co-transcriptionally.
1135

1136 **Figure 5. NRDE-3 switches small RNA targets during development.**

1137 A. Diagram of IP-sRNA seq on NRDE-3 early embryos (<=100-cell stage) and late embryos
1138 (>=300-cell). GFP::FLAG::NRDE-3 was immunoprecipitated from embryo lysate and its
1139 associated small RNAs were isolated for sequencing.
1140 B. Box plots depicting $\log_2$(fold change small RNA abundance) in NRDE-3 IP compared to
1141 input for at least two biological replicates.
1142 C. Normalized NRDE-3-bound small RNA read distribution across a CSR-target gene (*ztf-*
1143 *27*) and an ERGO-target gene (Y37E11B.2) in early embryos, late embryos, and young
1144 adults. One representative replicate is shown.
1145 D. Normalized NRDE-3 IP compared to input small RNA reads in early embryos, late
1146 embryos, and young adults. CSR-target and ERGO-target genes are indicated in blue
1147 and red, respectively. One representative replicate is shown. Insets are pie charts
1148 describing numbers of CSR targets, ERGO targets, and other targets that are
1149 significantly enriched in the NRDE-3 IP. The enriched targets were defined as small
1150 RNAs with at least 2-fold enrichment in IP compared to input, average RPM >10, and p-
1151 values ≤0.05.
1152 E. Normalized NRDE-3 IP compared to input small RNA reads in *eri-1* mutant early and
1153 late embryos. CSR-target and ERGO-target genes are indicated in blue and red,
1154 respectively. One representative replicate is shown.
1155 F. Box plots depicting $\log_2$(fold change small RNA abundance) in mutants compared to
1156 wild-type in early embryos for two or three biological replicates.
1157 G. Normalized NRDE-3 IP compared to input small RNA reads in *simr-1* mutant and *enri-2*
1158 mutant late embryos. CSR-target and ERGO-target genes are indicated in blue and red,
1159 respectively. One representative replicate is shown.
1160 H. Box plots depicting $\log_2$(fold change of ERGO-class small RNA abundance) in NRDE-3
1161 IP compared to input in wild-type and mutants in late embryos for two or three biological
1162 replicates.

1163 For box plots in B,F,H, bolded midline indicates median value, box indicates the first and
1164 third quartiles, and whiskers represent the most extreme data points within 1.5 times the

1165 interquartile range, excluding outliers. Two-tailed t-tests were performed to determine
1166 statistical significance and p-values were adjusted for multiple comparisons.
1167
1168 **Figure 6. NRDE-3 associates with CSR-class 22G-RNA in early embryos.**
1169 A. Live imaging of GFP::3xFLAG::NRDE-3 in one-day-adult germlines for wild-type, *eri-1*,
1170 *rde-3*, and *nrde-3(HK-AA)* mutants, showing that NRDE-3 localizes to the nuclei of
1171 oocytes in wild-type, *eri-1* mutant, and *rde-3* mutants, and to the cytoplasm in the *nrde-*
1172 *3(HK-AA)* mutant. At least five individual gonads were imaged for each genotype. Dotted
1173 white line traces the proximal portion of the *C. elegans* gonad and outlines the individual
1174 oocytes. Scale bars, 25 μm.
1175 B. Live imaging of one-day-adult germlines and 8-cell embryos for degron::EGO-1;
1176 GFP::3xFLAG::NRDE-3 in a *rde-3* mutant with ethanol (top) and 4mM auxin (bottom)
1177 treatment, showing that loss of both WAGO-class and CSR-class 22G-RNAs (*rde-3*
1178 mutant and degron-mediated EGO-1 depletion) leads to cytoplasmic localization of
1179 NRDE-3 in both oocytes and early embryos. At least five individual gonads and embryos
1180 were imaged for each treatment condition. Dotted white line traces the proximal portion
1181 of the *C. elegans* gonad and outlines the individual oocytes. Scale bars, 25 μm in adults
1182 and 5 μm in embryos.
1183 C. Venn diagrams indicate overlap of NRDE-3 IP enriched targets in early embryos (this
1184 work), CSR-1 IP enriched targets in young adults (Nguyen *et al.*, 2021), and CSR-1 IP
1185 enriched targets in embryos (Quarato *et al.*, 2021).
1186 D. Density plot of small RNA enrichment on CSR targets in CSR-1 IP (dark blue), NRDE-3
1187 IP (light blue) in embryos (top) and adults (bottom). Transcription start site (TSS) to
1188 transcription end site (TES) were plotted using normalized small RNA reads. All
1189 replicates are shown as individual lines.
1190 E. Box plots depicting normalized $\log_2$(fold change of small RNA abundance in IP vs input)
1191 in a NRDE-3 IP in early embryos and CSR IP in embryos for two or three biological
1192 replicates. All genes list includes all genes expressed in IP or input. Early degraded
1193 mRNAs are maternal mRNAs that show at least twofold reduction in mRNA levels in
1194 early embryos (4 to 20 cell-stage) compared to 1-cell embryos (Quarato *et al.*, 2021).
1195 Late degraded mRNAs are maternal mRNAs that show stable levels of mRNAs in early
1196 embryos and at least twofold reduction in late embryos (more than 20-cell stage)
1197 (Quarato *et al.*, 2021). Zygotic mRNAs are mRNAs that are not detectable in 1-cell
1198 embryos but accumulate in early and late embryos (Quarato *et al.*, 2021).

1199 F. Box plot quantifying the number of embryos laid per adult *csr-1::degron* or *csr::degron,*
1200 *gfp::nrde-3(HK-AA)* animal on 4mM auxin plate. At least 65 individuals from each strain
1201 were scored. Each dot represents an individual animal, and all data points are shown.
1202 G. Box plot depicting $\log_2$(fold change of H3K9me3 level in IP vs input) in wild-type (grey)
1203 and *nrde-3* mutant (green) mixed-stage embryos, indicating that the H3K9me3 level of
1204 NRDE-3 targets in early embryos are not affected in *nrde-3* mutant. Anti-H3K9me3
1205 ChIP-seq data was obtained from Padeken *et al.* (2021).
1206 For box plots in E,F,G, bolded midline indicates median value, box indicates the first and
1207 third quartiles, and whiskers represent the most extreme data points within 1.5 times the
1208 interquartile range, excluding outliers. Two-tailed t-tests were performed to determine
1209 statistical significance and p-values were adjusted for multiple comparisons.
1210
1211 **Figure 7. Model of the function of cytoplasmic granules in *C. elegans* development.**
1212 Model of NRDE-3, SIMR-1, and CSR-1 function during *C. elegans* development. In early
1213 embryos, CSR-1 and EGO-1 localize to CSR granules and synthesize CSR 22G-RNAs
1214 to slice and clear maternal mRNAs. NRDE-3 binds CSR 22G-RNA in the nucleus and
1215 may transcriptionally silence germline-expressed genes. During mid-embryogenesis
1216 (e.g. around the 100-cell stage), unloaded NRDE-3, ENRI-2, RRF-1, and RDE-3 are
1217 recruited to SIMR granules in somatic cells by SIMR-1, where ERGO-dependent 22G-
1218 RNAs are produced and loaded to NRDE-3. In late embryos, NRDE-3 binds ERGO-
1219 dependent 22G-RNAs and silences ERGO-target genes in the nucleus. In adult *C.*
1220 *elegans*, somatic localized NRDE-3 associates with ERGO-dependent 22G-RNAs to
1221 transcriptionally silence ERGO-target genes, while germline localized NRDE-3
1222 associates with CSR-class 22G-RNAs, possibly for deposition into early embryos.

A

mass spectrometry interactions				
	SIMR-1	NRDE-3	ENRI-2	ENRI-1
SIMR-1 IP (adult)	NA	2/3	0/3	0/3
NRDE-3 IP (embryo)	2/5	NA	2/5	5/5
ENRI-2 IP (embryo)	3/3	3/3	NA	0/3
ENRI-1 IP (embryo)	0/3	3/3	0/3	NA

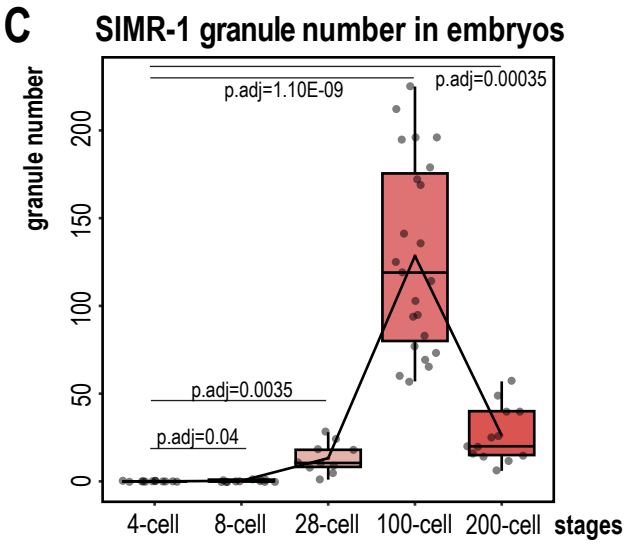

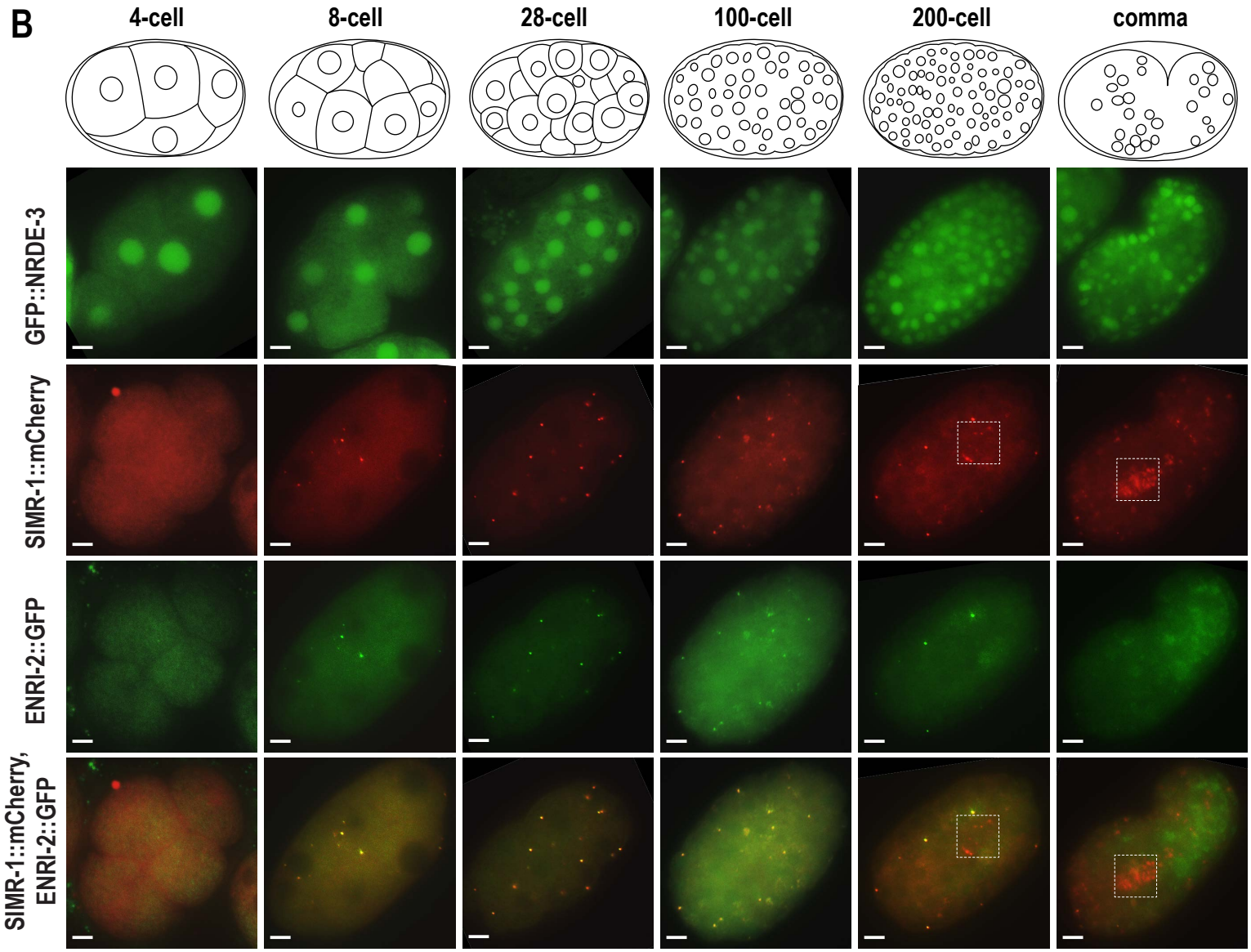

Figure 1. SIMR-1 and ENRI-2 colocalize at somatic granules in embryos.

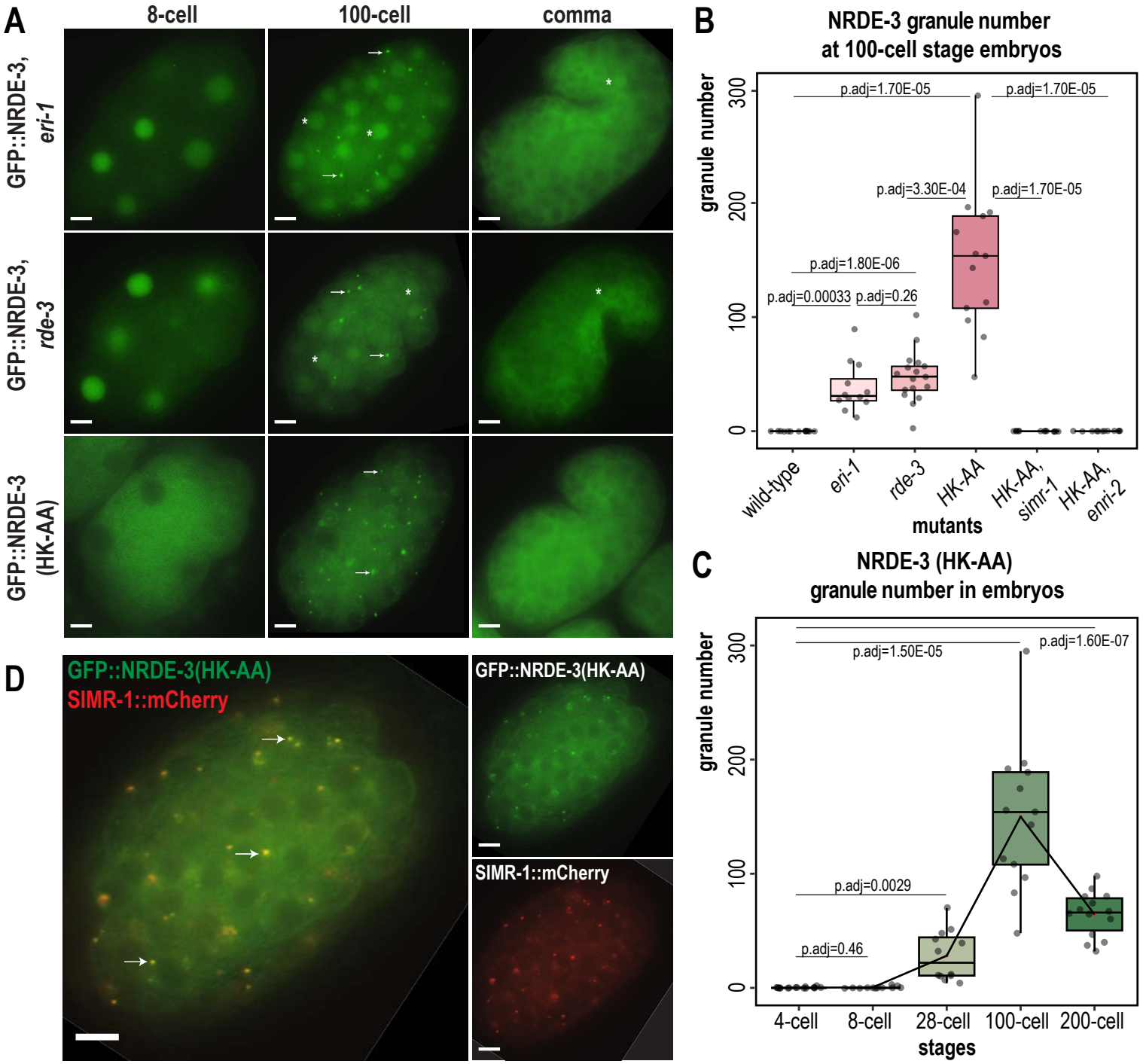

Figure 2. Unloaded NRDE-3 localizes to cytoplasmic granules with SIMR-1.

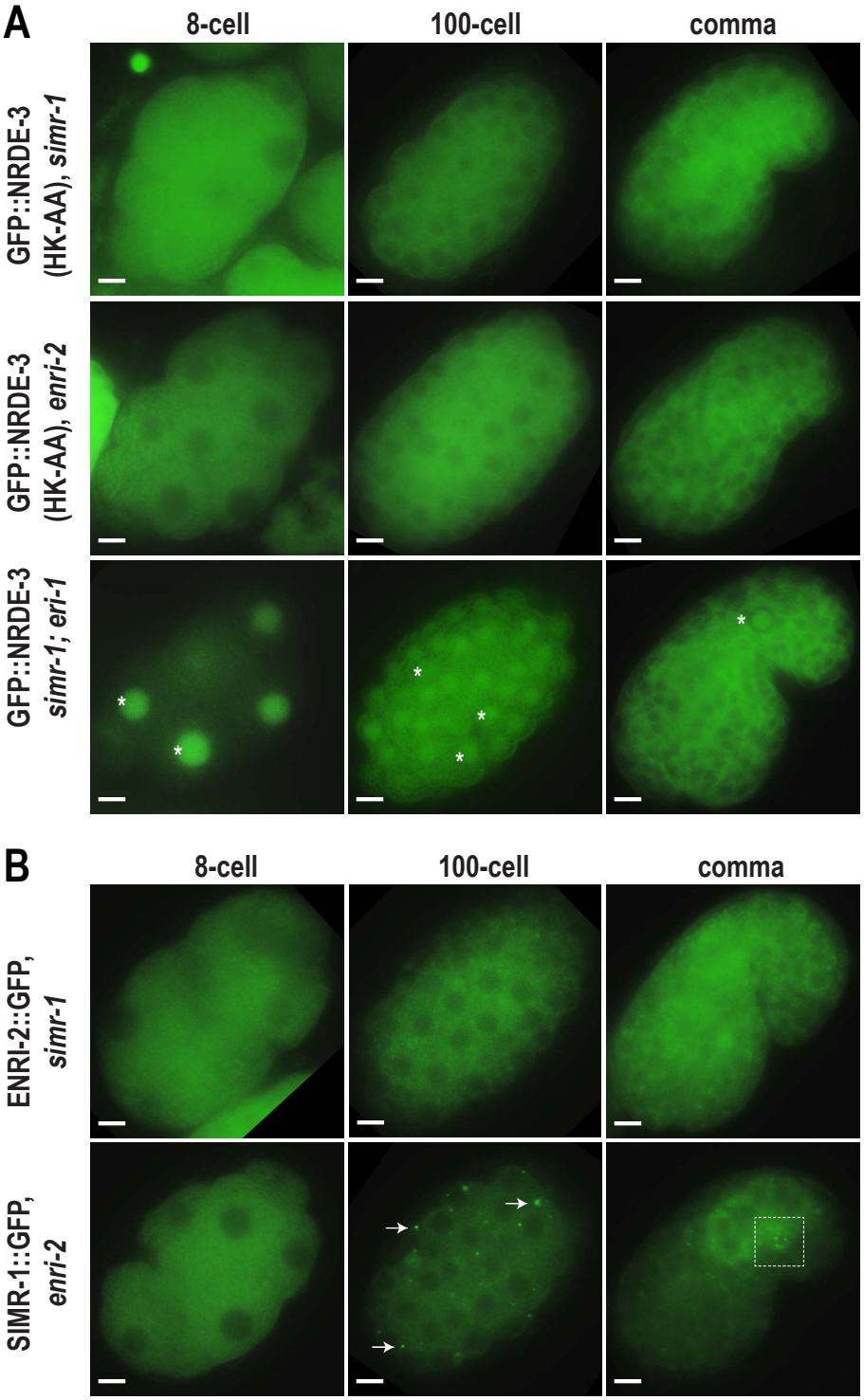

Figure 3. SIMR-1 recruits ENRI-2 and then NRDE-3 to cytoplasmic granules.

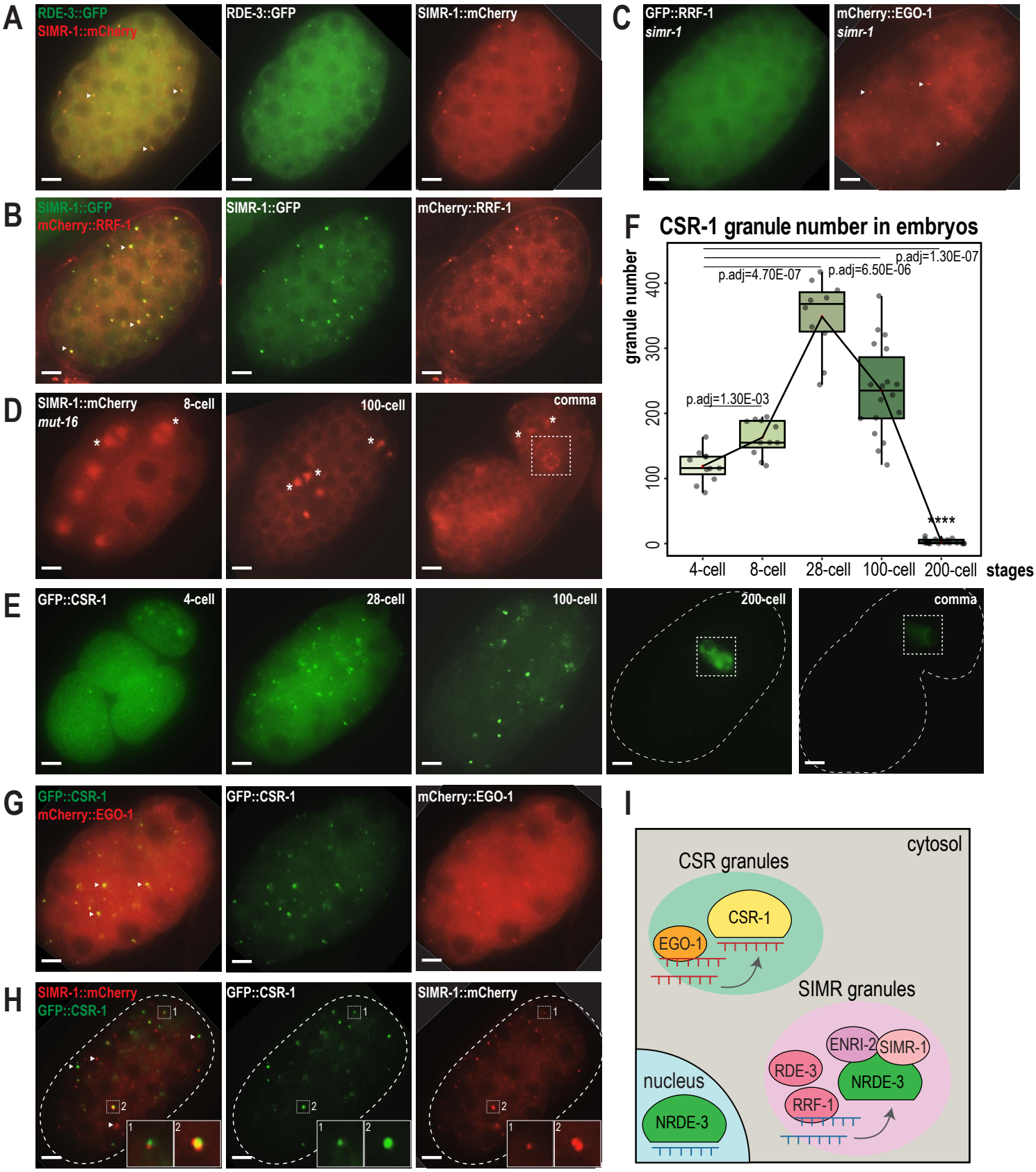

Figure 4. CSR and WAGO pathway proteins localize to distinct cytoplasmic granules.

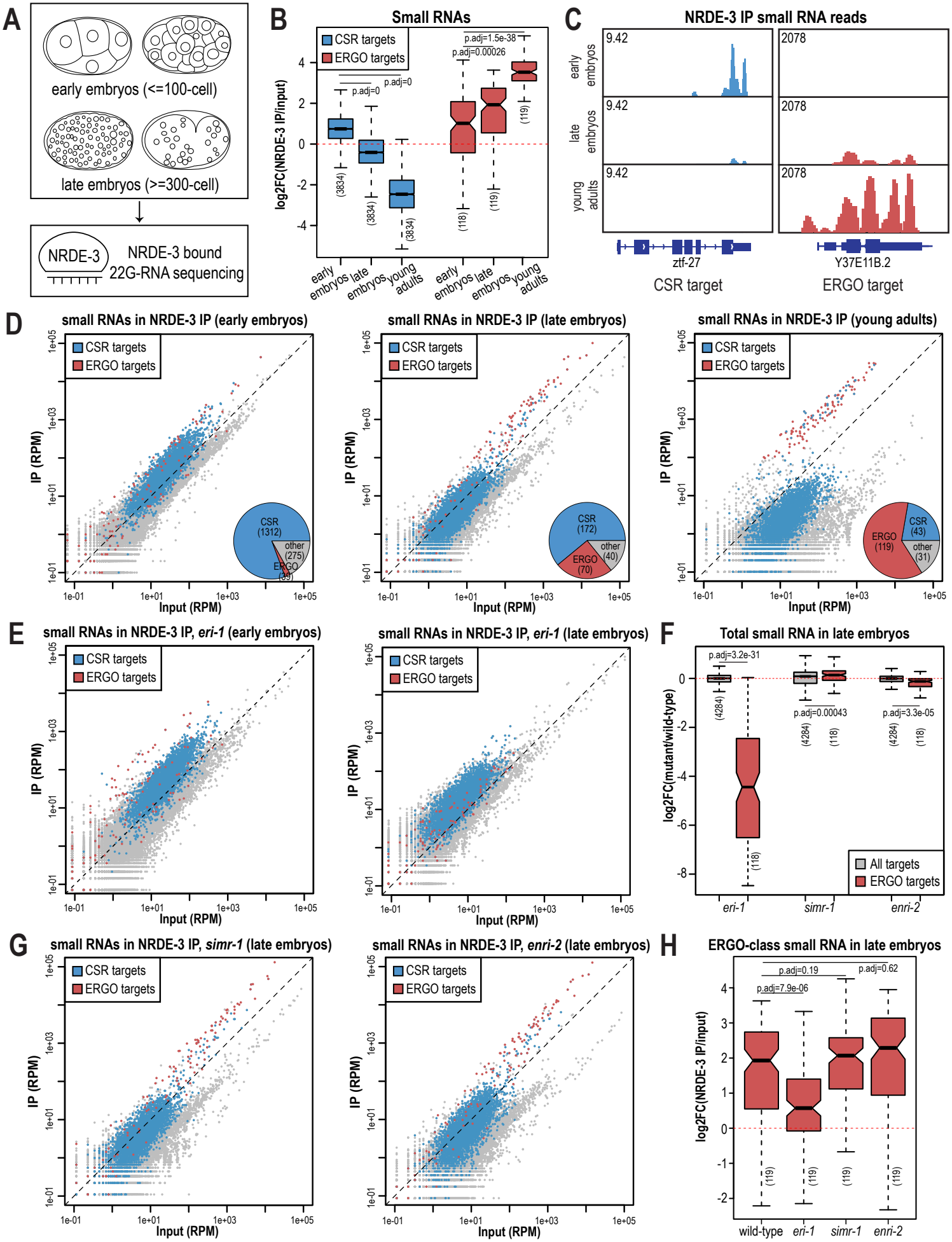

Figure 5. NRDE-3 switches small RNA targets during development.

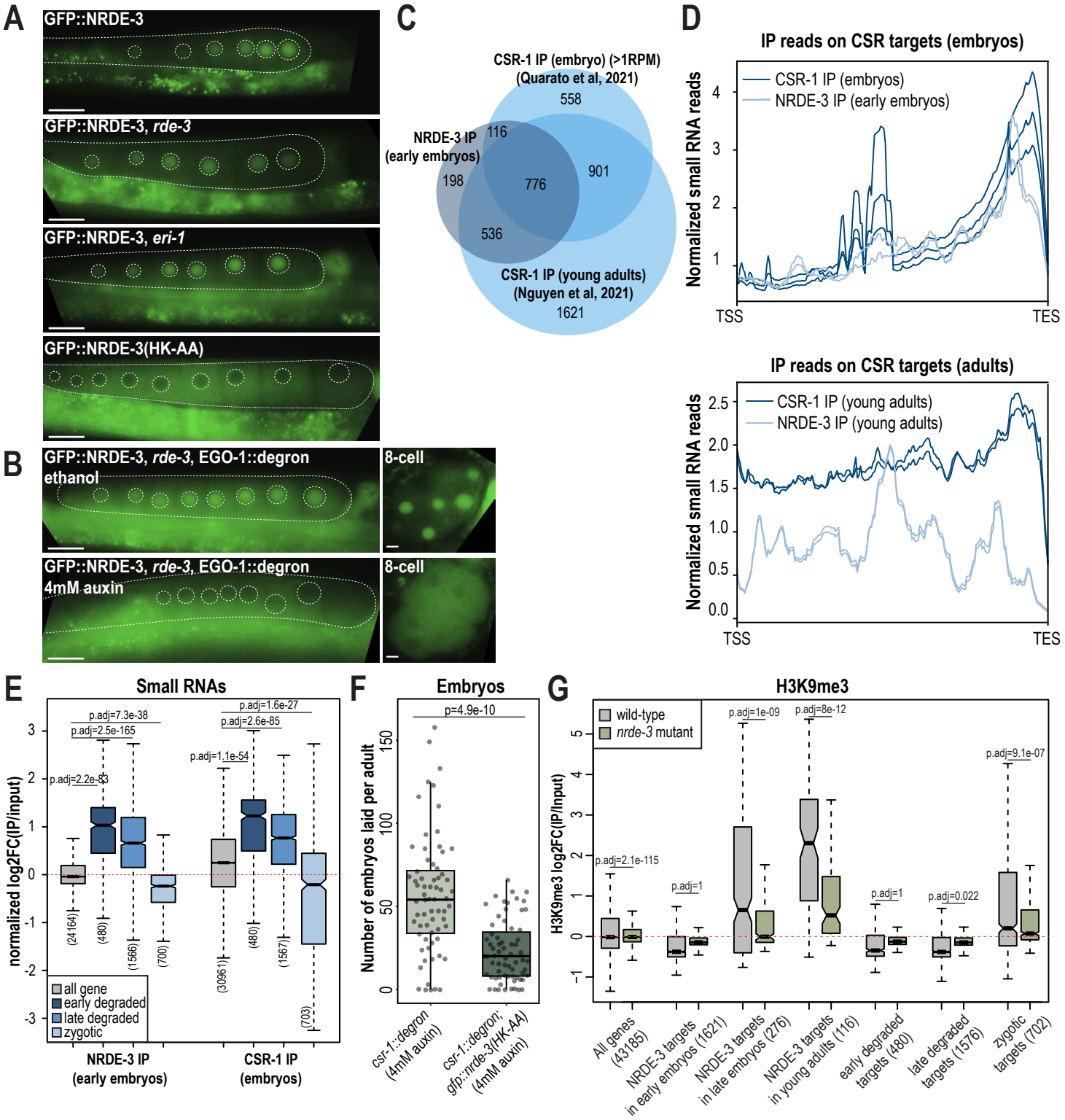

Figure 6. NRDE-3 associates with CSR-class 22G-RNA in early embryos.

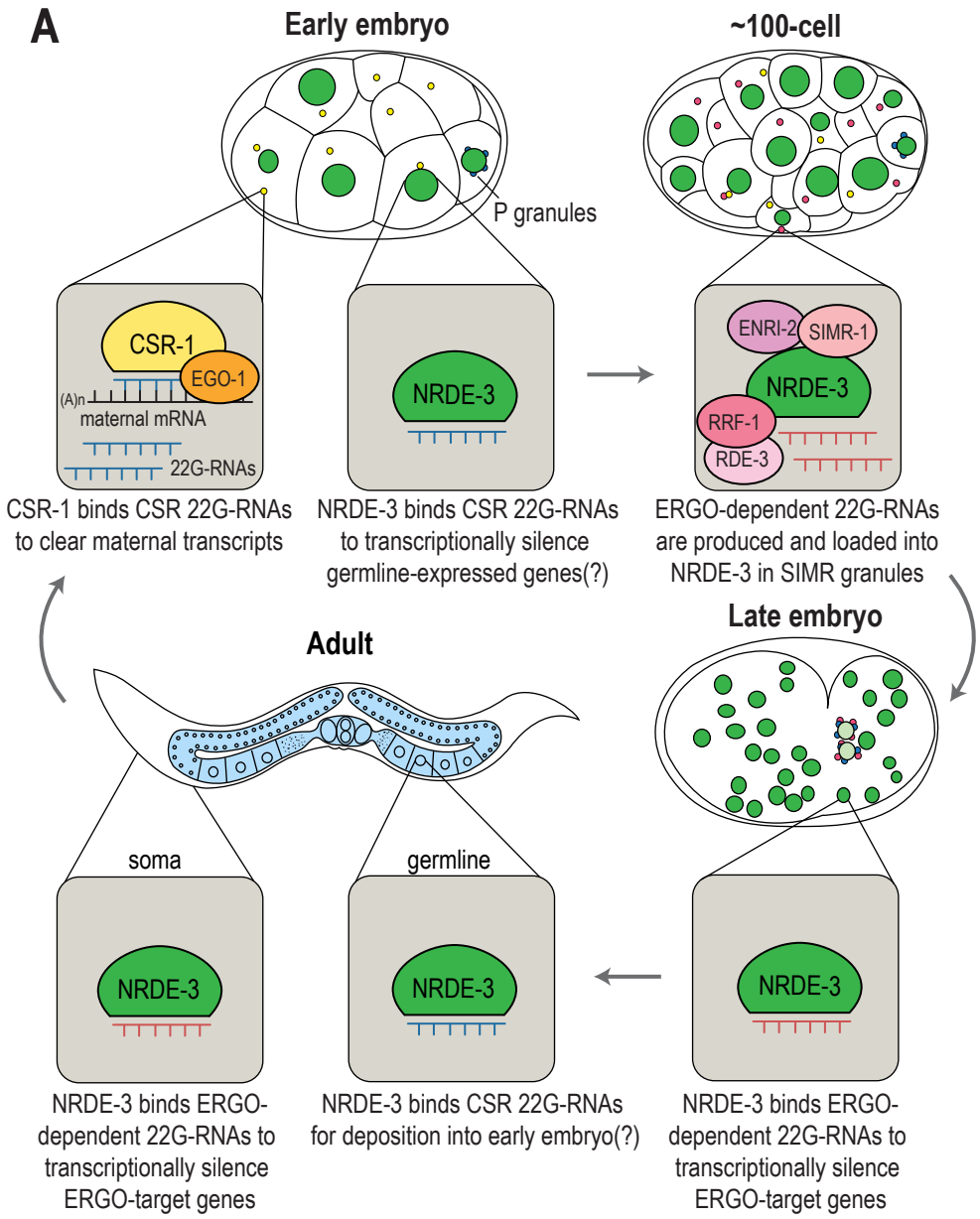

Figure 7. Function of cytoplasmic granules in *C. elegans* development.